The ALMA Survey of 70 μm Dark High-mass Clumps in Early Stages (ASHES). I. Pilot Survey: Clump Fragmentation

(article starts on next page)

The ALMA Survey of 70 μm Dark High-mass Clumps in Early Stages (ASHES). I. Pilot Survey: Clump Fragmentation

Patricio Sanhueza[1] , Yanett Contreras[2] , Benjamin Wu[1] , James M. Jackson[3] , Andrés E. Guzmán[1] , Qizhou Zhang[4] ,
Shanghuo Li[4,5,6] , Xing Lu[1] , Andrea Silva[1] , Natsuko Izumi[1,7] , Tie Liu[5] , Rie E. Miura[1] , Ken'ichi Tatematsu[1] ,
Takeshi Sakai[8] , Henrik Beuther[9] , Guido Garay[10] , Satoshi Ohashi[1,11] , Masao Saito[1] , Fumitaka Nakamura[1] , Kazuya Saigo[1] ,
V. S. Veena[12] , Quang Nguyen-Luong[1,13] , and Daniel Tafoya[14]

[1] National Astronomical Observatory of Japan, National Institutes of Natural Sciences, 2-21-1 Osawa, Mitaka, Tokyo 181-8588, Japan; patricio.sanhueza@nao.ac.jp
[2] Leiden Observatory, Leiden University, P.O. Box 9513, NL-2300 RA Leiden, The Netherlands
[3] SOFIA Science Center, USRA, NASA Ames Research Center, Moffett Field, CA 94045, USA
[4] Harvard-Smithsonian Center for Astrophysics, 60 Garden Street, Cambridge, MA 02138, USA
[5] Shanghai Astronomical Observatory, Chinese Academy of Sciences, 80 Nandan Road, Shanghai 200030, People's Republic of China
[6] University of Chinese Academy of Sciences, 19A Yuquanlu, Beijing 100049, People's Republic of China
[7] College of Science, Ibaraki University, 2-1-1 Bunkyo, Mito, Ibaraki 310-8512, Japan
[8] Graduate School of Informatics and Engineering, The University of Electro-Communications, Chofu, Tokyo 182-8585, Japan
[9] Max Planck Institute for Astronomy, Königstuhl 17, D-69117, Heidelberg, Germany
[10] Departamento de Astronomía, Universidad de Chile, Camino el Observatorio 1515, Las Condes, Santiago, Chile
[11] RIKEN Cluster for Pioneering Research, 2-1, Hirosawa, Wako-shi, Saitama 351-0198, Japan
[12] Physikalisches Institut, Universität zu Köln, Zülpicher Str. 77, D-50937 Köln, Germany
[13] IBM Canada, 120 Bloor Street East, Toronto, ON, M4Y 1B7, Canada
[14] Department of Space, Earth and Environment, Chalmers University of Technology, Onsala Space Observatory, SE-439 92 Onsala, Sweden

Abstract

The ALMA Survey of 70 μm dark High-mass clumps in Early Stages (ASHES) is designed to systematically characterize the earliest stages and constrain theories of high-mass star formation. Twelve massive (>500 $M_\odot$), cold ($\leqslant 15$ K), 3.6–70 μm dark prestellar clump candidates, embedded in infrared dark clouds, were carefully selected in the pilot survey to be observed with the Atacama Large Millimeter/submillimeter Array (ALMA). We have mosaicked each clump (~ 1 arcmin^2) in continuum and line emission with the 12 m, 7 m, and Total Power (TP) arrays at 224 GHz (1.34 mm), resulting in $\sim 1''.2$ resolution (~ 4800 au, at the average source distance). As the first paper in the series, we concentrate on the continuum emission to reveal clump fragmentation. We detect 294 cores, from which 84 (29%) are categorized as protostellar based on outflow activity or "warm core" line emission. The remaining 210 (71%) are considered prestellar core candidates. The number of detected cores is independent of the mass sensitivity range of the observations and, on average, more massive clumps tend to form more cores. We find a large population of low-mass (<1 $M_\odot$) cores and no high-mass (>30 $M_\odot$) prestellar cores (maximum mass 11 $M_\odot$). From the prestellar core mass function, we derive a power-law index of 1.17 ± 0.10, which is slightly shallower than Salpeter. We used the minimum spanning tree (MST) technique to characterize the separation between cores and their spatial distribution, and to derive mass segregation ratios. While there is a range of core masses and separations detected in the sample, the mean separation and mass per clump are well explained by thermal Jeans fragmentation and are inconsistent with turbulent Jeans fragmentation. Core spatial distribution is well described by hierarchical subclustering rather than centrally peaked clustering. There is no conclusive evidence of mass segregation. We test several theoretical conditions and conclude that overall, competitive accretion and global hierarchical collapse scenarios are favored over the turbulent core accretion scenario.

Unified Astronomy Thesaurus concepts: Infrared dark clouds (787); Dust continuum emission (412); Star forming regions (1565); Massive stars (732); Star formation (1569)

Supporting material: machine-readable tables

1. Introduction

Several key questions in high-mass star formation focus on the early fragmentation of prestellar massive clumps.[15] Prestellar cores embedded in massive clumps at any evolutionary stage are rare, and their observational characterization is ultimately needed to constrain model predictions. Are prestellar core masses segregated, with the more massive cores preferentially located toward the clump center? Do high-mass prestellar cores ($\gtrsim 30$ $M_\odot$) exist early on? Is the prestellar core mass function (CMF) Salpeter-like? All these basic questions have not been possible to address in the past yet are a necessary step before digging in to the detailed internal physics and chemistry of prestellar cores at $\lesssim 1000$ au scales, as has been recently done in nearby, low-mass prestellar cores (Ohashi et al. 2018; Caselli et al. 2019). High-mass stars form in clustered environments, and the initial imprints of the core spatial distribution and mass segregation, as well as the prestellar CMF, found at the early clump fragmentation are important components for cluster formation simulations.

---

[15] Consistent with Sanhueza et al. (2017), throughout this work we use the term "clump" to refer to a dense object within an infrared dark cloud with a size of the order ~ 0.2–1 pc, a mass of $\sim 10^2$–10^3 $M_\odot$, and a volume density of $\sim 10^4$–10^5 cm^{-3} that will form a stellar cluster. We use the term "core" to describe a compact, dense object within a clump with a size of ~ 0.01–0.1 pc, a mass of $\sim 10^{-1}$–10^2 $M_\odot$, and a volume density of $\gtrsim 10^5$ cm^{-3} that will form a single star or close binary system.

Theories that attempt to explain the formation mechanisms of clusters along with high-mass stars fall into two broad categories: "clump fed" and "core fed." In the "clump-fed" category, competitive accretion scenarios (Bonnell et al. 2004; Bonnell & Bate 2006; Smith et al. 2009; Wang et al. 2010) and global hierarchical collapse (Heitsch et al. 2008; Vázquez-Semadeni et al. 2009, 2017, 2019; Ballesteros-Paredes et al. 2011a, 2011b, 2018) are included, which are mostly consistent with each other (Vázquez-Semadeni et al. 2019, see this work for a detailed discussion on the similarities and differences). These scenarios are characterized by global clump infall, and simulations predict the formation of clusters along with high-mass stars. Fragmentation produces low-mass cores (∼Jeans mass) that acquire mass through gas infall from their parent structures (clumps). Those cores, preferentially located near the center of the forming cluster gravitational potential, increase their masses to become massive enough to form high-mass stars. Given that the cores at early times have masses near the Jeans mass, the CMF evolves due to accretion to become the universal initial mass function (IMF) later on. In these "clump-fed" scenarios, the core distribution is expected to be hierarchical, and because the cores that are the seeds of high-mass stars are near the center of the gravitational potential of the cluster-forming clump, primordial mass segregation is predicted (e.g., Bonnell & Bate 2006).

Conversely, the "core-fed" turbulent core accretion scenario (McKee & Tan 2003) treats the formation of high-mass stars in isolated environments rather than as part of cluster formation, but it is supported by numerical simulations of cluster formation (e.g., Krumholz et al. 2012; Myers et al. 2014). In the turbulent core accretion model, global infall is gradual (Tan et al. 2006), allowing quasi-equilibrium structures during their assembly, and does not contribute to the core mass. The core mass is fixed at the early fragmentation and, because the core is near virial equilibrium, the core mass is approximately constant over time. In order to form high-mass stars, high-mass prestellar cores must exist (Tan et al. 2013, 2014). Therefore, turbulent core accretion theory predicts a direct relationship between the CMF and the IMF. The CMF would resemble the IMF but shifted to higher masses by an efficiency factor that would be independent of the core mass (similar to what has been postulated in nearby, low-mass star-forming regions; e.g., Alves et al. 2007; André et al. 2010; Könyves et al. 2015). No specific prediction is made on the spatial core distribution, and Tan (2018) points out that the massive cores may or may not be at the center of cluster-forming clumps (therefore, no specific prediction on primordial mass segregation). However, numerical simulations that reproduce the predicted accretion rates from this scenario find primordial mass segregation (Myers et al. 2014). These outlines of the high-mass star formation scenarios oversimplify their physical and chemical complexity. For finer details, the following reviews by Krumholz & Bonnell (2009), Tan et al. (2014), and Vázquez-Semadeni et al. (2019) are suggested.

Comprehensive studies to address the previously posed questions and to test theories backed by large samples have been historically challenging, mostly due to two factors. First, it is difficult to identify prestellar, massive clump candidates that can form high-mass stars. Second, after selecting suitable targets, the detection of the weak dust and molecular line emission of the cold, distant candidates require time-expensive observations at high angular resolution, precluding systematical studies of large samples until recently. Before the Atacama Large Millimeter/submillimeter Array (ALMA) era, high-angular-resolution studies of massive clumps at early evolutionary stages mostly targeted individual regions with the Submillimeter Array (SMA), Plateau de Bure Interferometer (PdBI, now NOEMA), Combined Array for Research in Millimeter-wave Astronomy (CARMA), and Very Large Array (VLA) in different array configurations and gas tracers that made analysis taken as a whole complicated (e.g., Zhang et al. 2009; Pillai et al. 2011, 2019; Wang et al. 2012, 2014; Sanhueza et al. 2013, 2017; Beuther et al. 2015; Lu et al. 2015; Feng et al. 2016a, 2016b). ALMA has finally made possible the study of large samples to achieve statistically significant conclusions in a uniform fashion (e.g., similar array configurations, analysis strategies, and gas tracers).

The preferred targets to study the earliest stages of high-mass star formation are infrared dark clouds (IRDCs), molecular clouds seen as dark silhouettes against the Galactic 8 μm mid-infrared background in Galactic plane surveys, e.g., using *MSX* in Simon et al. (2006) and *Spitzer* in Peretto & Fuller (2009). Among IRDCs, those that are also 24 and 70 μm dark are colder and denser than other IRDCs (Guzmán et al. 2015) and are believed to trace the earliest stages of high-mass star formation (Sanhueza et al. 2013, 2017; Tan et al. 2013; Contreras et al. 2018). However, lack of 24 and 70 μm emission does not guarantee a complete absence of star formation activity (e.g., Tan et al. 2016; Feng et al. 2016b; Li et al. 2019a). Several studies have investigated the kinematics and filamentary structure of IRDCs (Busquet et al. 2013; Foster et al. 2014; Henshaw et al. 2014, 2016; Liu et al. 2014, 2018b; Ragan et al. 2015; Contreras et al. 2016; Lu et al. 2018; Chen et al. 2019), their chemistry (Sakai et al. 2008, 2012, 2015; Sanhueza et al. 2012, 2013; Hoq et al. 2013; Miettinen 2014; Vasyunina et al. 2014; Feng et al. 2016a; Kong et al. 2016; Tatematsu et al. 2017), molecular outflow content (Sanhueza et al. 2010; Wang et al. 2011, 2014; Lu et al. 2015; Kong et al. 2019; Li et al. 2019b), infall (Sanhueza et al. 2010; Contreras et al. 2018; Liu et al. 2018c), magnetic fields (Pillai et al. 2015; Beuther et al. 2018b; Juvela et al. 2018; Liu et al. 2018c; Tang et al. 2019), and in the more-evolved ones, ultracompact (UC) H II regions (Battersby et al. 2010; Avison et al. 2015), thermal ionized jets (Rosero et al. 2014, 2016, 2019), hot cores (Rathborne et al. 2008; Sakai et al. 2013; Csengeri et al. 2018), and maser emission (Pillai et al. 2006; Wang et al. 2006; Chambers et al. 2009; Yanagida et al. 2014).

IRDC clumps that lack star formation indicators (UC H II regions, molecular outflows, hot cores, maser emission) are prime candidates to be in the prestellar phase. Although the source selection in this work is explained in detail in Section 2, the selection of prestellar massive clump candidates generally consists of the following combined effort at different wavelengths: (i) categorization of prestellar/protostellar phase based on large IR surveys, GLIMPSE (Benjamin et al. 2003) based on *Spitzer*/IRAC 3–8 μm emission, MIPSGAL (Carey et al. 2009) based on *Spitzer*/MIPS 24–70 μm emission, and Hi-GAL (Molinari et al. 2010) using *Herschel*/PACS 70 μm emission, (ii) clump mass and temperature calculation using SED fitting of dust emission usually from Hi-GAL *Herschel*/SPIRE 250–500 μm and ATLASGAL using APEX 870 μm (e.g., Guzmán et al. 2015; Traficante et al. 2015; Contreras et al. 2017), (iii) kinematical information to obtain distances

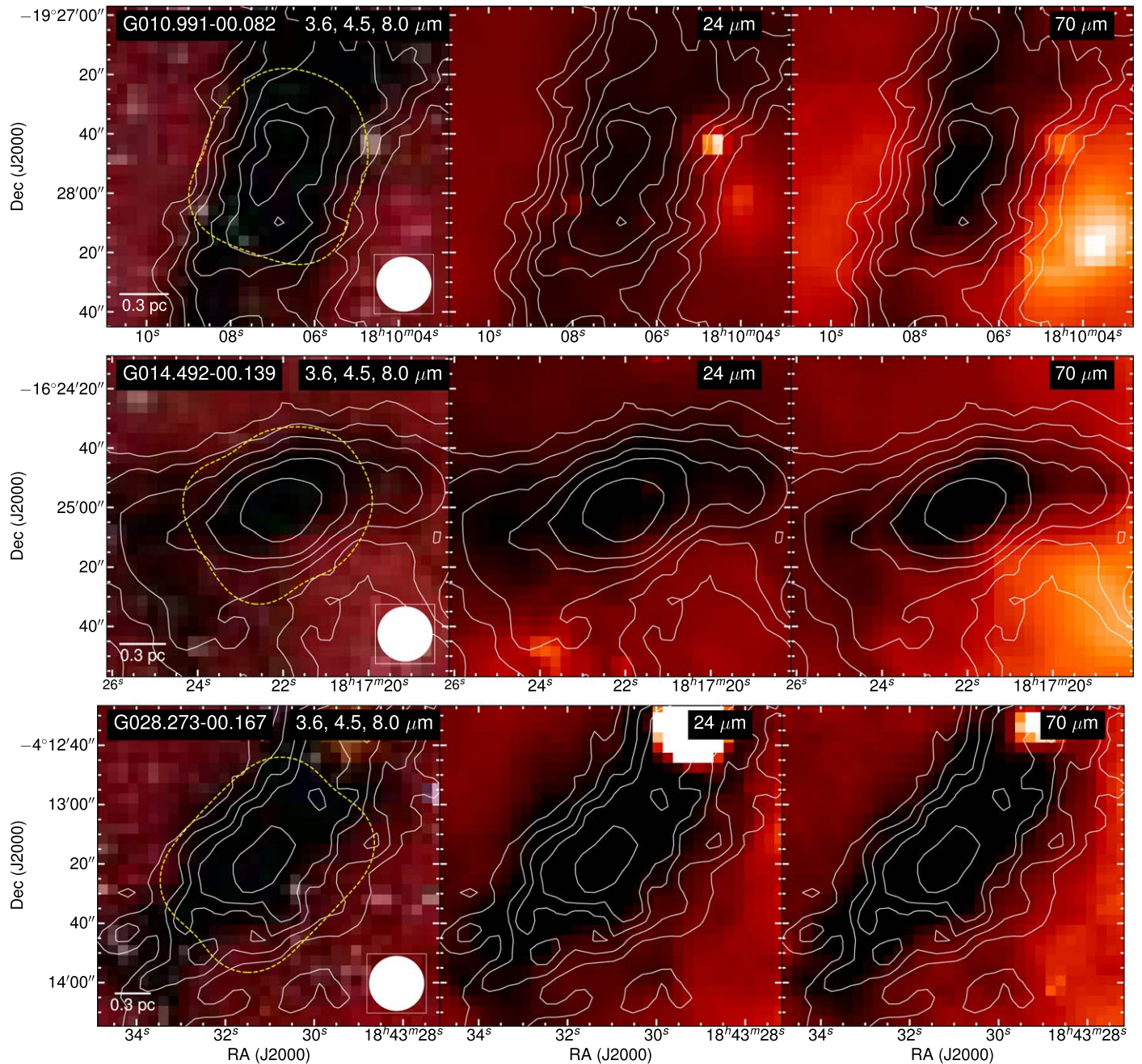**Figure 1.** *Spitzer* and *Herschel* IR images for the observed IRDC clumps overlaid with 870 μm dust continuum emission from the ATLASGAL survey (19″.2; shown on the bottom right of the first panel) in white contours. Left: *Spitzer*/IRAC three-color (3.6 μm in blue, 4.5 μm in green, and 8.0 μm in red) image. Dashed yellow contour delineates the area mosaicked with ALMA. Center: *Spitzer*/MIPS 24 μm image. Right: *Herschel*/PACS 70 μm image. Contour levels for the 870 μm dust continuum emission are 3, 5, 7, 9, 12, and 15 $\times$ σ, with $\sigma = 71.8$ mJy beam^{-1}, for G010.991–00.082; 3, 6, 9, 13, 17, and 25 $\times$ σ, with $\sigma = 82.7$ mJy beam^{-1}, for G014.492–00.139; and 3, 5, 7, 9, and 12 $\times$ σ, with $\sigma = 64.9$ mJy beam^{-1}, for G028.273–00.167.

and hints of active star formation (based on outflows, chemistry, maser detection, high-temperatures) from large molecular line surveys, e.g., MALT90 (Foster et al. 2011; Jackson et al. 2013), Shirley et al. (2013), Wienen et al. (2015), and RAMPS (Hogge et al. 2018).

In this work, we present the pilot Alma Survey of 70 μm dark High-mass clumps in Early Stages (ASHES). A deep understanding of high-mass star formation requires the study of the clustered mode, which is the most commonly found in nature. We have therefore mosaicked 12 prestellar, massive clump candidates in dust continuum and molecular line

emission at $\sim$224 GHz ($\sim$1″.2 resolution) using the 12 m, 7 m, and TP arrays of ALMA. Here we focus on clump fragmentation, using the dust continuum emission to characterize the earliest stages of high-mass star formation and constrain theory. The core dynamics, based on an analysis of C^{18}O, DCO^{+}, and N$_2$D^{+} emission, is presented in a companion paper (Y. Contreras et al. 2019, in preparation). Following the approach delineated in Li et al. (2019a), the molecular outflow content will be presented by S. Li et al. (2019, in preparation). "Warm core" line emission will be presented by N. Izumi et al. (2019, in preparation).
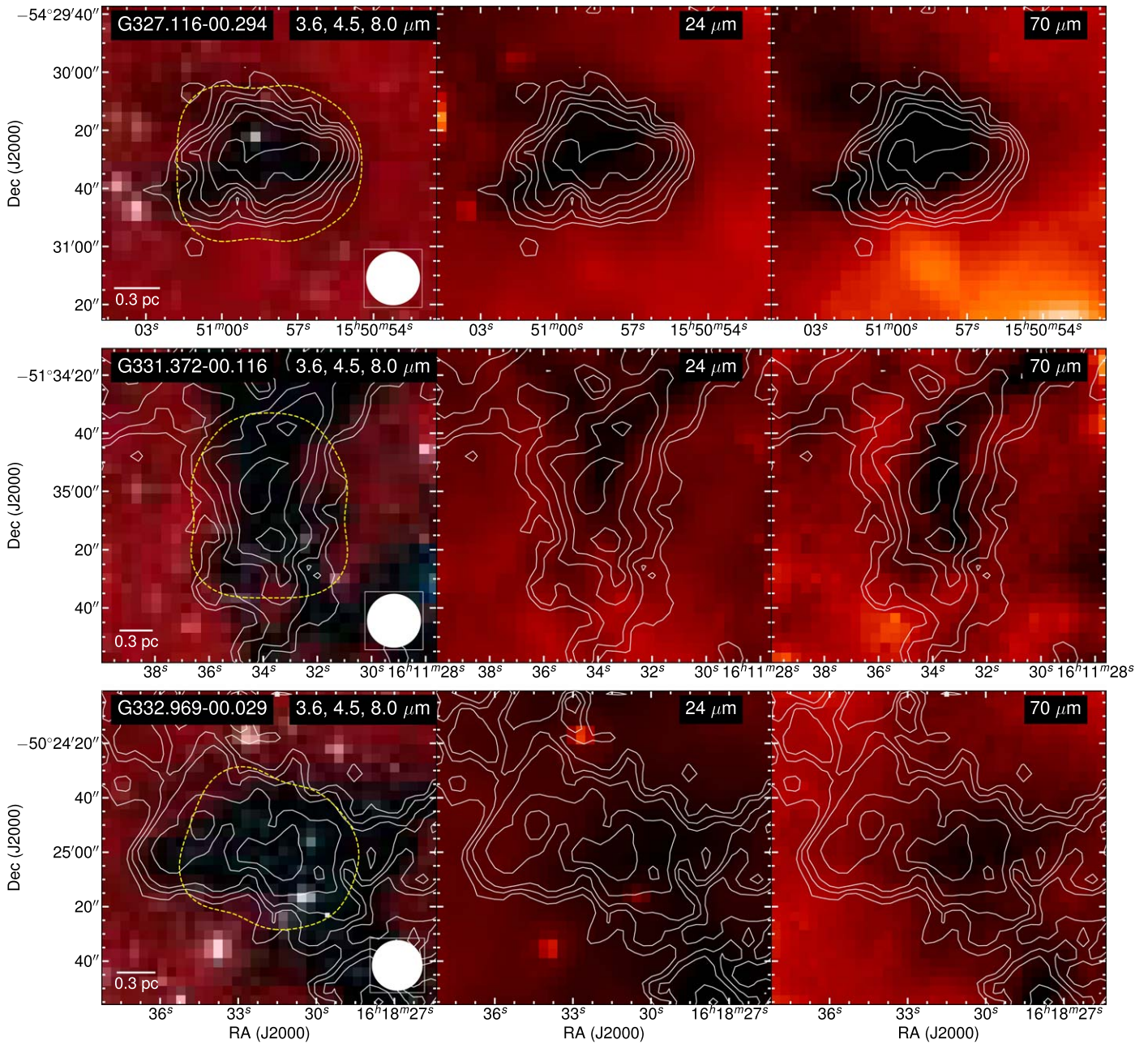
Figure 2. Same as in Figure 1, except for contour levels for the 870 μm dust continuum emission, which are 3, 4, 5, 6, 7, and 9 × σ, with σ = 70.9 mJy beam^{-1}, for G327.116–00.294; 3, 4, 6, 8, and 10 × σ, with σ = 56.5 mJy beam^{-1}, for G331.372–00.116; and 3, 4, 5, 7, and 9 × σ, with σ = 46.9 mJy beam^{-1}, for G332.969–00.029.

2. Source Selection: Prestellar 70 μm dark, High-mass Clump Candidates

The identification of prestellar 70 μm dark, high-mass (>500 $M_\odot$) clump candidates has substantially improved with the advent of *Spitzer* and *Herschel* satellites and ground-based dust continuum and molecular line surveys. For the ASHES pilot survey, 11 IRDC clumps were selected from the Millimetre Astronomy Legacy Team 90 GHz Survey (MALT90; Foster et al. 2011, 2013; Jackson et al. 2013). MALT90 was built on the ATLASGAL 870 μm catalogs (Schuller et al. 2009; Contreras et al. 2013), from which a sample of 3246 high-mass clumps was selected for follow-up in 16 spectral lines. The first MALT90 line catalog was presented in Rathborne et al. (2016), and several

studies have taken advantage of the molecular line data (e.g., Hoq et al. 2013; Miettinen 2014; He et al. 2015, 2016; Stephens et al. 2015, 2016; Yu & Wang 2015; Contreras et al. 2016; Jackson et al. 2018, 2019; Li et al. 2019c, 2019d). By combining *Herschel* and ATLASGAL dust continuum emission observations, Guzmán et al. (2015) derived temperatures and column densities for the MALT90 survey targets. After determining clump kinematical distances (Whitaker et al. 2017), masses and number densities were calculated by Contreras et al. (2017). With all these vast ancillary multiwavelength data sets, we made a careful selection of prestellar clump candidates that will potentially form high-mass stars.

In Guzmán et al. (2015), we first identify IR-dark clumps from 3.6 to 70 μm in *Spitzer/Herschel* (see Figures 1–4). The
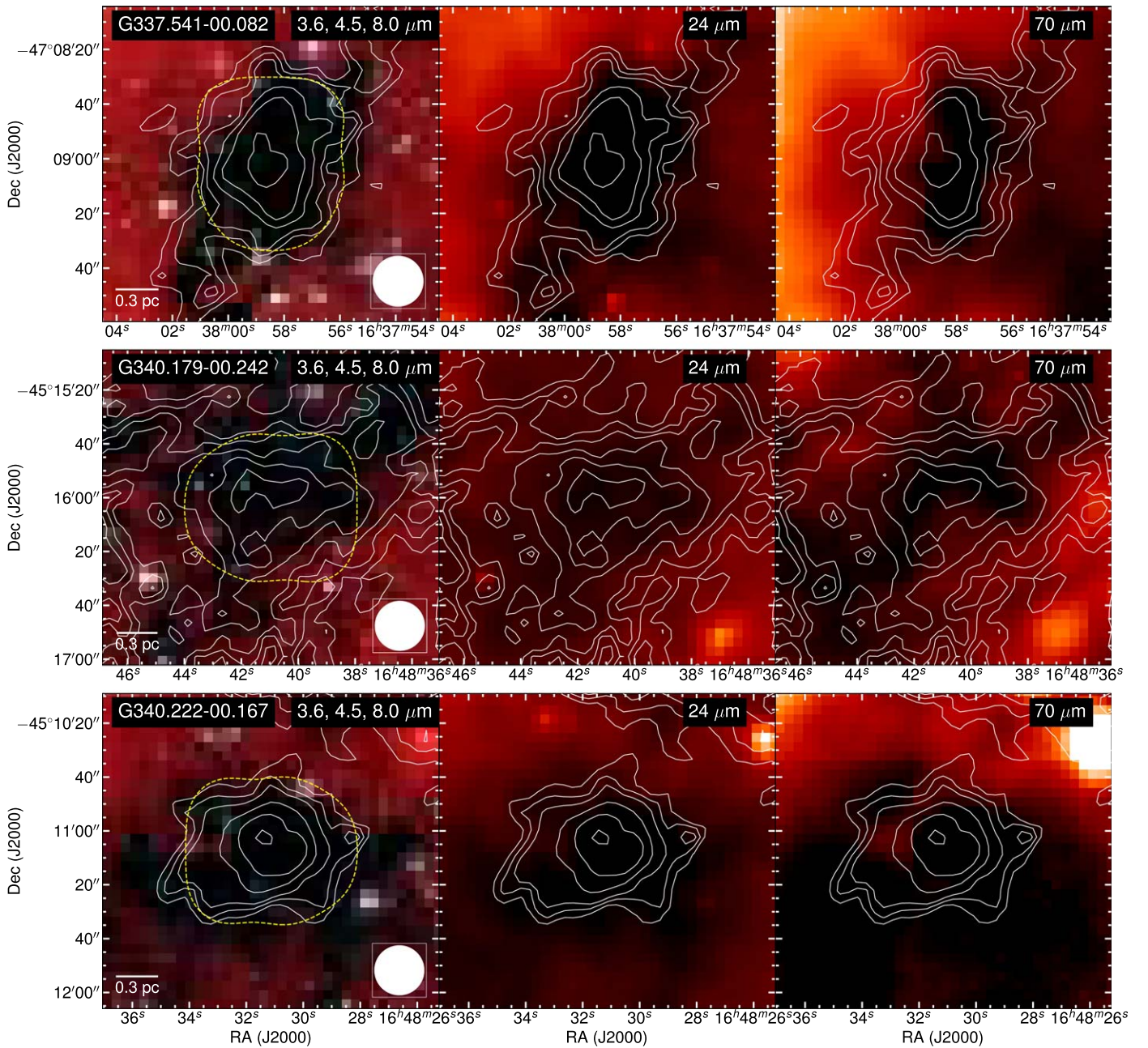
Figure 3. Same as in Figure 1, except for contour levels for the 870 μm dust continuum emission, which are 3, 4, 5, 7, 9, and 12 × σ, with $\sigma = 66.3$ mJy beam^{-1}, for G337.541–00.082; 3, 4, 5, 7, 9, and 11 × σ, with $\sigma = 57.3$ mJy beam^{-1}, for G340.179–00.242; and 3, 4, 5, 7, 9, and 12 × σ, with $\sigma = 65.7$ mJy beam^{-1}, for G340.222–00.167.

presence of IR compact emission indicates embedded sources in the protostellar phase, while their absence makes the clump a prestellar candidate. From 3246 sources, only 83 sources fulfill the latter requirement. This small fraction of potentially prestellar clumps demonstrates the rarity, and presumably, short lifetime of the high-mass prestellar phase. To ensure the selection of the best prestellar candidates with sufficient mass to form high-mass stars, we impose additional selection criteria. Clumps must have (1) dust temperatures equal to or lower than the average temperature of the 70 μm dark subsample, i.e., $\leqslant 15$ K, (2) masses larger than 500 $M_\odot$, (3) have number densities $\gtrsim 10^4$ cm^{-3}, and (4) molecular line emission from MALT90 consistent with cold gas, i.e., no shock (SiO) or hot

core (HC$_3$N, CH$_3$CN, and HNCO) emission. To ensure good spatial resolution, an additional constraint is that the targets should be closer than 5.5 kpc. Only 18 sources satisfy these conditions, and 11 were observed in this pilot survey. The 12th target in the ASHES pilot survey is G028.273–00.167, which is in the first quadrant and was not covered in MALT90. This IRDC satisfies all previous requirements and has been well studied in the past by Sanhueza et al. (2012, 2013, 2017). Key physical properties for all 12 IRDC clumps are listed in Table 1: columns (1–3) contain clump names with their coordinates, columns (4–5) contain the $V_{\rm lsr}$ and velocity dispersion of the gas (σ) determined by using high-density tracers with critical densities $>10^5$ cm^{-3}, and columns (6–8)
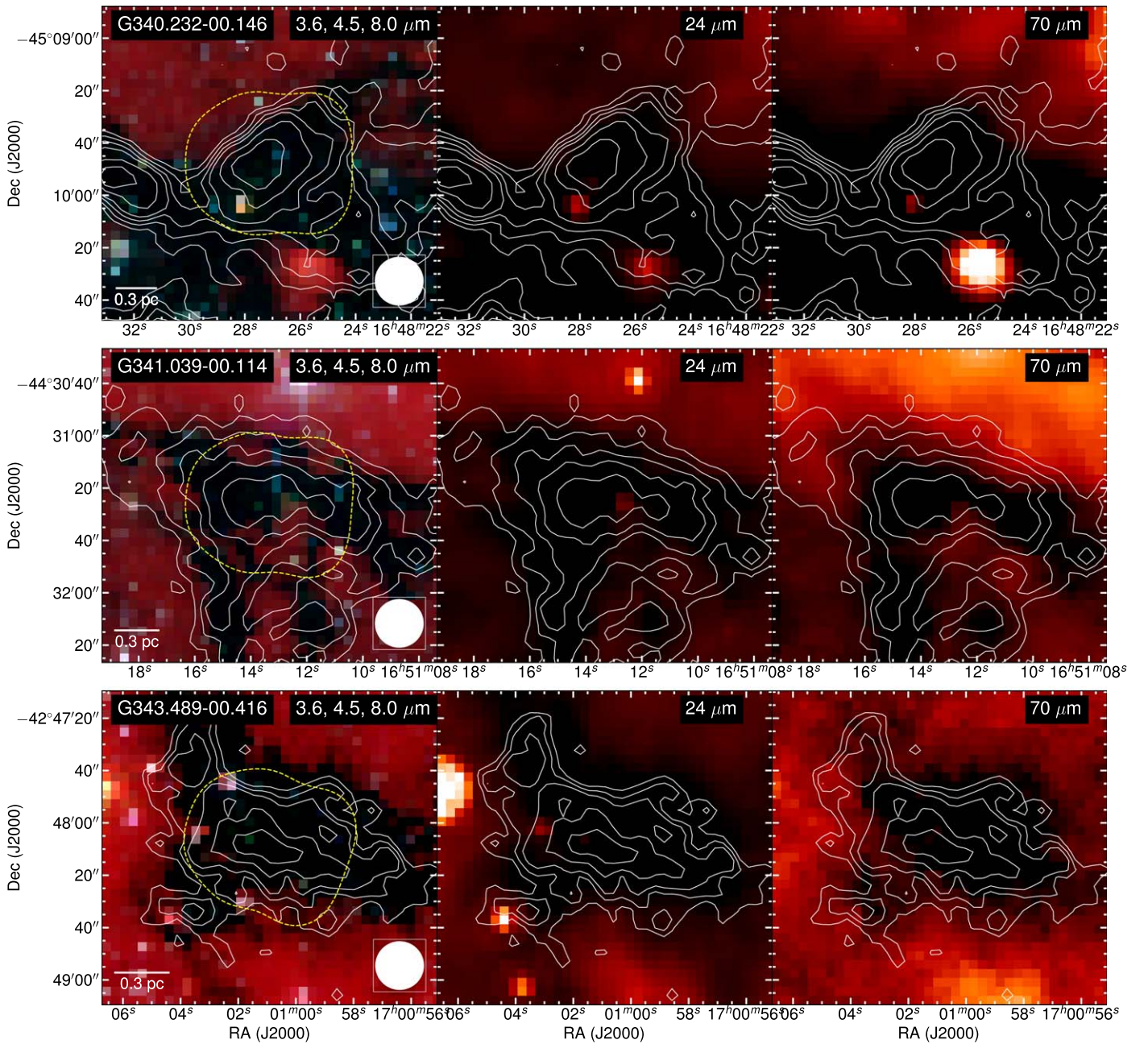
Figure 4. Same as in Figure 1, except for contour levels for the 870 μm dust continuum emission, which are 3, 4, 5, 6, 8, and 10 $\times$ σ, with $\sigma = 65.1$ mJy beam^{-1}, for G340.232–00.146; 3, 5, 7, 9, and 12 $\times$ σ, with $\sigma = 52.2$ mJy beam^{-1}, for G341.039–00.114; and 3, 4, 5, 7, and 9 $\times$ σ, with $\sigma = 53.9$ mJy beam^{-1}, for G343.489–00.416.

are the clump properties considered for target selection (see further details in the notes of Table 1). Columns (9–12) are described in the following paragraph.

While the source selection was based on the MALT90 properties, we refine the size and mass of the clumps to be more representative of the observed region with ALMA. We determine clump sizes by performing Gaussian fitting to the ATLASGAL 870 μm dust emission maps and define R_{cl}, column (9) in Table 1, as the geometric mean of the semimajor and semiminor FWHMs . Consequently, we scale the MALT90 mass to a new clump mass M_{cl}, column (10) in Table 1, based on the measured integrated flux from the Gaussian fitting and the flux inside the mask defining the MALT90 source. R_{cl} and

M_{cl}, which also define the surface density (Σ_{cl}) and volume density ($n_{cl}(H_2)$) in columns (11–12) in Table 1, will be used throughout this work.

We note that all of our target clumps had a single velocity component in MALT90 data, while the sensitive C^{18}O $J = 2$–1 ALMA observations reveal in most clumps more than one velocity component along the line of sight. Based on the integrated intensity of C^{18}O, Contreras et al. (2018) estimated that the mass of G331.372–00.116 could be 75% of the value previously reported by Contreras et al. (2017) using *Herschel* observations. We checked the C^{18}O $J = 2$–1 emission in the remaining 11 clumps and confirmed that, except for G332.969–00.029 which could have its mass reduced by $\sim$50%, clumps have contamination of <10%

Table 1
Physical Properties of the Prestellar, High-mass Clump Candidates

IRDC[a] Clump (1)	Position[b] α(J2000) (2)	δ(J2000) (3)	V_{lsr} (km s^{-1}) (4)	σ[c] (km s^{-1}) (5)	Dist. (kpc) (6)	T_{dust} (K) (7)	Mass ($M_\odot$) (8)	R_{cl} (pc ["]) (9)	M_{cl} ($M_\odot$) (10)	Σ_{cl} (g cm^{-2}) (11)	$n_{cl}(H_2)$ ($\times 10^4$ cm^{-3}) (12)
G010.991–00.082	18:10:06.65	−19.27.50.7	29.5	1.27	3.7	12.0	2230	0.49 (27)	1810	0.50	5.3
G014.492–00.139	18:17:22.03	−16.25.01.9	41.1	1.68	3.9	13.0	5200	0.44 (23)	3120	1.1	13
G028.273–00.167	18:43:31.00	−04.13.18.1	80.0	0.81	5.1	12.0	1520	0.59 (24)	1520	0.28	2.4
G327.116–00.294	15:50:57.18	−54.30.33.6	−58.9	0.56	3.9	14.3	580	0.39 (20)	580	0.26	3.5
G331.372–00.116	16:11:34.10	−51.35.00.1	−87.8	1.29	5.4	14.0	1640	0.63 (24)	1230	0.20	1.7
G332.969–00.029	16:18:31.61	−50.25.03.1	−66.6	1.41	4.4	12.6	730	0.59 (28)	530	0.10	0.9
G337.541–00.082	16:37:58.48	−47.09.05.1	−54.6	2.01	4.0	12.0	1180	0.42 (22)	1040	0.40	5.0
G340.179–00.242	16:48:40.88	−45.16.01.1	−53.7	1.48	4.1	14.0	1470	0.74 (37)	1020	0.12	0.9
G340.222–00.167	16:48:30.83	−45.11.05.8	−51.3	3.04	4.0	15.0	760	0.36 (19)	720	0.38	5.5
G340.232–00.146	16:48:27.56	−45.09.51.9	−50.8	1.23	3.9	14.0	710	0.48 (25)	520	0.15	1.7
G341.039–00.114	16:51:14.11	−44.31.27.2	−43.0	0.97	3.6	14.3	1070	0.47 (27)	850	0.26	2.9
G343.489–00.416	17:01:01.19	−42.48.11.0	−29.0	1.00	2.9	10.3	810	0.42 (29)	790	0.30	3.8

Notes. Properties in columns (6), (7), and (8) were used for source selection. Clump properties for G028.273–00.167, also known as G028.23–00.19, were derived by Sanhueza et al. (2012, 2013). Clump properties for G010.991–00.082 and G014.492–00.139 were calculated using the column densities from Guzmán et al. (2015) and the distances derived according to Whitaker et al. (2017). Clump properties for the remaining nine clumps were derived and presented in a series of works by the MALT90 team: Guzmán et al. (2015, temperatures), Rathborne et al. (2016, V_{lsr}), Contreras et al. (2017, masses), and Whitaker et al. (2017, distances). Due to multiple velocities along the line of sight, and based on the C^{18}O emission, the masses of G331.372–00.116 and G332.969–00.029 could be lower by ~25% and ~50%, respectively. Properties in columns (9), (10), (11), and (12) are used for clump analysis through this work. R_{cl} was derived from Gaussian fitting to the dust continuum emission from ATLASGAL and M_{cl} scaled from column (8) using the integrated flux derived in the Gaussian fitting. The clump surface density, column (11), is calculated as $\Sigma_{cl} = M_{cl}/\pi R_{cl}^2$. The volume density, column (12), was calculated assuming a spherical clump of radius R_{cl} and using the molecular weight per hydrogen molecule (μ_{H_2}) of 2.8.
[a] By replacing G in the IRDC name for AGAL, the name of the source has the same nomenclature as in the ATLASGAL catalog (Schuller et al. 2009).
[b] Phase center for ALMA mosaics. Due to the positioning of the mosaic, the phase center and the ATLASGAL catalog coordinates are slightly different in few arcsecs.
[c] Velocity dispersion was obtained using NH$_2$D $J_{K_a,K_b} = 1_{1,1}-1_{0,1}$ emission for G028.273–00.167, HNC $J = 1$–0 emission for G337.541–00.082 and G340.222–00.167, and N$_2$H$^+$ $J = 1$–0 emission for the remaining nine clumps. All three molecular tracers have critical densities $>10^5$ cm^{-3} (Sanhueza et al. 2012).

of the mass derived using *Herschel* observations (which is within ~50% uncertainty of the mass determination).

Assuming a star-cluster formation efficiency of 18% (Lada & Lada 2003), the least massive clump (G340.232–00.146 with $M_{cl} = 520\,M_\odot$) should form a stellar cluster of 94 $M_\odot$. Following Equations (1) and (2)[16] in Sanhueza et al. (2017), based on the empirical relation from Larson (2003) and the IMF from Kroupa (2001), we estimate that G340.232–00.146 should form a high-mass star of 8–9 $M_\odot$. The most massive clump, G014.492–00.139 ($M_{cl} = 3120\,M_\odot$), with a stellar cluster of 562 $M_\odot$, should form a high-mass star of 21–29 $M_\odot$. All IRDC clumps are above the empirical high-mass star formation thresholds from Kauffmann & Pillai (2010), Urquhart et al. (2014), and He et al. (2015). Kauffmann & Pillai (2010) suggest that clumps with masses larger than $m_{lim} = 580\,M_\odot$ $(r/\text{pc})^{1.33}$, where r is the source radius, are currently forming or will likely form high-mass stars. The values for m_{lim} range from 150 to 390 $M_\odot$, all lower than the clump masses, which indicate that it is highly likely that the clumps will form high-mass stars. Both Urquhart et al. (2014) and He et al. (2015) propose that high-mass stars form in clumps with $\Sigma_{clump} > 0.05$ gr cm^{-2}. All Σ_{cl} listed in Table 1 satisfy this threshold as well. Therefore, each source selected for this pilot survey exhibits the necessary physical properties likely to form a stellar cluster hosting at least

one high-mass star. Thus, this overall sample is suitable for the characterization of the earliest stages of high-mass star formation.

3. Observations

Observations of the 12 IRDCs were carried out with ALMA on different days during Cycle 3 (Project ID: 2015.1.01539.S; PI: Sanhueza) and a resubmission for Cycle 4 (Project ID: 2016.1.01246.S; PI: Sanhueza). The data sets consist of observations in band 6 (~224 GHz; 1.34 mm) with the main 12 m array, the Atacama Compact 7 m Array (ACA; Morita Array), and the total power (TP). Table 2 summarizes all observational parameters.

Total 12 m array time on source per mosaic for sources that were observed in one execution is ~16 minutes (first six sources in Table 2), while sources that were observed in two executions have a total 12 m array time per mosaic of ~25 minutes. Total 7 m array observing time per mosaic is ~50 minutes, except for the first three sources in Table 2 that were observed longer (~100 minutes). Some sources were observed in different configurations, resulting in different angular resolutions (baselines are listed in Table 2). To have a more uniform data set, uv-taper was used in those observations with more extended baselines in order to achieve a similar synthesized beam of ~1.″2 for every source (see Table 2 for individual values). This angular resolution corresponds to a physical size of 4800 au (0.023 pc) at the average source distance of 4 kpc. At 224 GHz, the primary beams of the 12 m array and ACA are 25.″2 and 44.″6, respectively. These observations are sensitive to angular scales smaller than ~11″ and ~19″, respectively.

---

[16] In Sanhueza et al. (2017), Equation (2) has a typographical error that overestimated the maximum stellar mass by ~10%. The correct version is added in Appendix A of the present work. The lowest mass regime of the Kroupa (2001) formulation for the IMF has also been added.

Table 2
Observational Parameters

IRDC Clump	rms Noise[a] (mJy beam^{-1})	Beam Size[a] ($'' \times ''$)	Baselines[b] (m)	Configuration	Number of Antennas[c]
G010.991–00.082	0.115	1.29 × 0.86	15–330	C36-1	41 (9–10)
G014.492–00.139	0.168	1.29 × 0.85	15–330	C36-1	41 (9–10)
G028.273–00.167	0.164	1.28 × 1.20	15–462	C36-2/3	41 (8–10)
G327.116–00.294	0.089	1.32 × 1.11	15–330	C36-1	48 (8)
G331.372–00.116	0.083	1.34 × 1.09	15–330	C36-1	48 (8)
G332.969–00.029	0.080	1.35 × 1.08	15–330	C36-1	48 (8)
G337.541–00.082	0.068	1.29 × 1.18	15–639	C36-2/3–C40-1	41–43 (8–9)
G340.179–00.242	0.094	1.41 × 1.29	15–704	C36-2/3–C40-4	36–41 (8–9)
G340.222–00.167	0.112	1.40 × 1.28	15–704	C36-2/3–C40-4	36–41 (8–9)
G340.232–00.146	0.139	1.39 × 1.26	15–704	C36-2/3–C40-4	36–41 (8–9)
G341.039–00.114	0.070	1.30 × 1.18	15–639	C36-2/3–C40-1	41–43 (8–9)
G343.489–00.416	0.068	1.30 × 1.18	15–639	C36-2/3–C40-1	41–43 (8–9)

Notes.
[a] Continuum sensitivity and synthesized beam in the combined 12 and 7 m data sets.
[b] For the 7 m array, the baselines range from 8 to 48 m.
[c] Values in parentheses refer to the number (or range) of antennas for the 7 m array. Ranges are given when there is more than one execution block with a different number of antennas.

With one exception, IRDCs were observed in continuum and line emission in Nyquist-sampled ten-pointing and three-pointing mosaics with the 12 m array and the ACA, respectively. IRDC G028.273–00.167 was observed with 11 and 5 pointings, respectively. Within the 20% power point, a ten-pointing mosaic corresponds to 0.97 arcmin^2 (1.06 arcmin^2 for IRDC G028.273–00.167), which is equivalent to an effective FOV of ~1′ per target. By using mosaics, we ensure coverage of a large area of clumps, as defined by single-dish continuum observations. The same correlator setup was used for all sources. The continuum emission was produced by averaging the line-free channels in visibility space. All images have 512 × 512 pixels, with a pixel size of 0″.2. To mitigate artifacts produced by the extended emission from IRDCs, we used TCLEAN and its MULTISCALE imaging option with scale values of 0, 5, 15, and 25 times the pixel size. Using Briggs weighting with a robust parameter of 0.5, the 1σ rms noise for the continuum emission is on average 0.10 mJy beam^{-1} (see Table 2 for each individual source).

At least 10 different molecular lines were included in the spectral setup (N$_2$D$^+$ $J = 3-2$, DCN $J = 3-2$, DCO$^+$ $J = 3-2$, CCD $J = 3-2$, ^{13}CS $J = 5-4$, SiO $J = 5-4$, C^{18}O $J = 2-1$, CO $J = 2-1$, H$_2$CO $J = 3-2$, and CH$_3$OH $J = 4-3$). The line sensitivity for the first six lines is ~9.5 mJy beam^{-1} per channel of 0.17 km s^{-1}, while for the last four lines it is ~3.5 mJy beam^{-1} per channel of 1.3 km s^{-1} (we note these channels correspond to the spectral resolution and not to the raw channel size, which is half of the spectral resolution, i.e., ~0.085 and ~0.65 km s^{-1}, respectively). We defer the analysis of all molecular lines to future papers. In this work, we analyze the dust continuum emission. We only use qualitative information of line emission for the classification of the evolutionary sequence of the cores (CO, SiO, H$_2$CO, and CH$_3$OH) and the determination of multiple velocity components on the line of sight (C^{18}O).

Calibration was carried out using CASA software package versions 4.5.3, 4.6, and 4.7, while imaging was done using CASA 5.4 (McMullin et al. 2007). All images presented in this paper are not primary beam corrected, but all fluxes are measured on the primary-beam-corrected images. We note that all targets were also observed with the TP antennas. However, TP antennas do not provide continuum emission and are therefore not used in this work.

4. Results

4.1. Dust Continuum Emission

Figures 5–10 show the 1.34 mm dust continuum images of the combined 12 and 7 m arrays. For comparison, the 870 μm dust continuum emission from the single-dish survey ATLASGAL is overlaid. ALMA dust continuum emission was successfully detected in all 12 targets. The small-scale structure resolved with ALMA presents different morphologies and is roughly in agreement with the single-dish emission delineated by ATLAS-GAL. Some sources are filamentary (e.g., G331.372–00.116 and G341.039–00.114), while others are rather clumpy (e.g., G028.273–00.167 and G340.232–00.146).

Integrating the flux over the compact and extended emission, the combined data sets (12 + 7 m) have between 1.1 and 7.1 (on average 2.6) times more flux than the 12 m-only images. All dust continuum images show more structures in the combined data sets (12 + 7 m) and, unless explicitly stated, all analyses will be carried out on the combined data sets. In the absence of continuum emission observations with a single-dish telescope at 1.34 mm, the 870 μm emission was scaled by assuming a dust emissivity spectral index (β) of 1.5 to estimate how much flux is recovered by ALMA. Consistent with SMA/ALMA observations in other IRDC studies (e.g., Wang et al. 2014; Sanhueza et al. 2017; Liu et al. 2018a), between 10% and 33% (average of 21%) of the single-dish emission is recovered. This relatively low flux recovery likely indicates that dust and gas in the clumps is distributed on large scales ($\gtrsim 20''$). Therefore, most of the mass at the earliest stages of high-mass star formation is diffuse and not (yet) confined in cores.
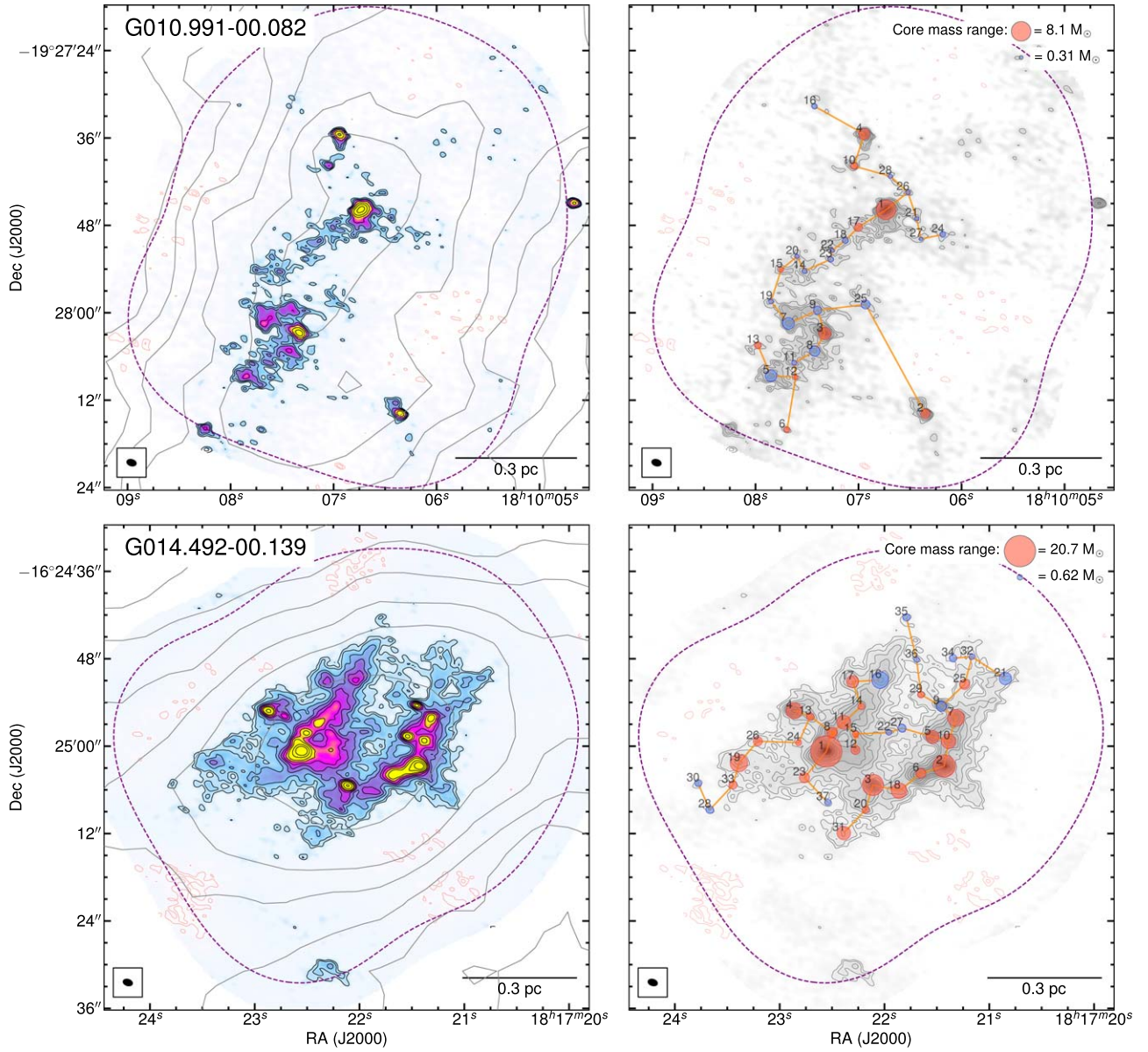
Figure 5. ALMA 1.34 mm dust continuum emission for two IRDC clumps. Dashed purple contour delineates the area mosaicked with ALMA. Left: color image and small-scale contours correspond to the ALMA dust continuum emission (12 and 7 m array combined). ALMA contour levels are −4, −3, 3, 4, 5, 7, 10, 14, and 20 × σ, with σ = 0.115 mJy beam^{-1}, for G010.991−00.082 (1″1 angular resolution); and −4, −3, 3, 4, 6, 8, 10, 12, 15, 18, 25, and 35 × σ, with σ = 0.168 mJy beam^{-1}, for G014.492−00.139 (1″1 angular resolution). Gray and red contours mark the positive and negative levels, respectively. Synthesized beams are displayed at the bottom left in each panel. Large-scale contours delineate the single-dish dust continuum emission from ATLASGAL (contour levels are the same as in the corresponding Figures 1, 2, 3, or 4). Right: grayscale image and contours correspond to the ALMA dust continuum emission (12 and 7 m array combined). Blue circles show the positions of the prestellar core candidates, while the red circles show the positions of the protostellar cores (see Section 4.3). The circle size is proportional to the core mass (centered at the emission peak), and the range of mass values is displayed on the upper-right corner of the panel. Numbers near each core correspond to the core name (ALMA1, ALMA2, ...), where the prefix ALMA has been dropped for clarity. Orange segments show the outcome from the minimum spanning tree (Section 5.4.1), which corresponds to the set of straight lines that connects cores in a way that minimizes the sum of the lengths.

4.2. Extraction of Core's Properties

To measure the integrated flux, peak flux, size, and position of cores from the dust continuum images, we adopted the dendrogram technique (Rosolowsky et al. 2008). An intensity threshold of 2.5σ, step of 1.0σ, and a minimum number of pixels equal to those contained in half of each synthesized beam were used to define the smaller structures called "leaves," which are defined as cores (σ equal to the rms noise in Table 2). Finally, cores with integrated flux densities smaller than 3.5σ were filtered to eliminate spurious detections. After core identification, all fluxes were corrected by the primary beam

response. A total of 301 cores were detected in the 12 IRDC clumps (an average of 25 cores per clump). On average, ∼26 cores per arcmin^2 are detected, which corrected by the clump distance implies ∼18 cores per pc^2. The number of cores identified in each IRDC ranges from 13 to 41. The broad range may indicate differences in the nature of each clump or just be related to the mass sensitivity, which depends on the flux sensitivity, temperature, and distance to the source (see Section 5.1 for the derivation of core mass). There is only a weak correlation between the flux sensitivity (rms in Table 2) and the number of cores identified, with a Spearman's rank
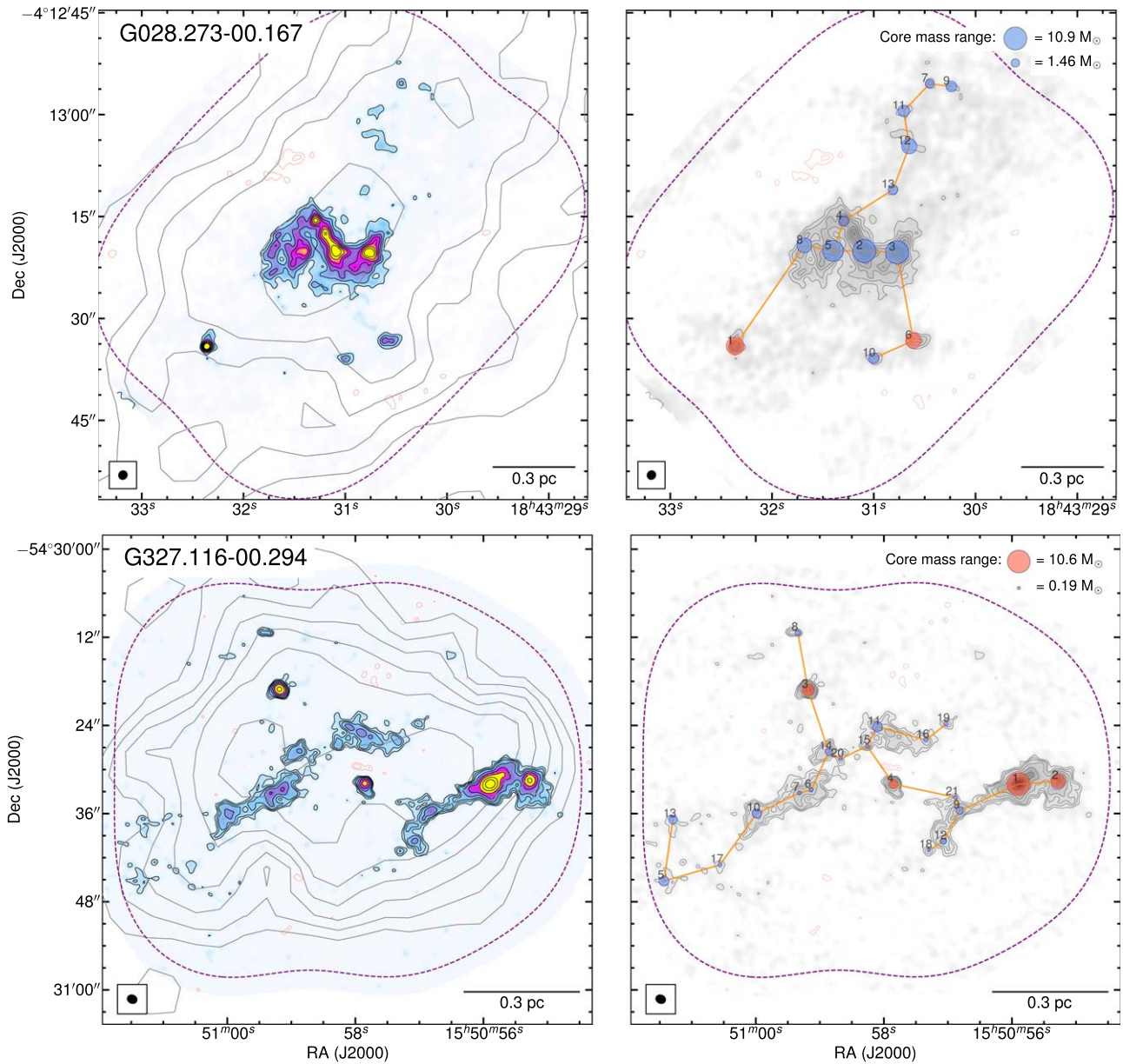
Figure 6. Same as in Figure 5, except for the ALMA contour levels of -4, -3, 3, 4, 5, 6, 7, 8, and 9 $\times\, \sigma$, with $\sigma = 0.164$ mJy beam^{-1}, for G028.273–00.167 (1$\farcs$2 angular resolution); and -4, -3, 3, 4, 5, 7, 10, 15, 23, and 35 $\times\, \sigma$, with $\sigma = 0.089$ mJy beam^{-1}, for G327.116–00.294 (1$\farcs$2 angular resolution).

correlation coefficient[17] of -0.16. The number of detected cores is uncorrelated with distance, with ρ_s equal to -0.06. As seen in Figure 11, the 3.5σ point-source mass sensitivity has no correlation with the number of cores identified over this threshold, with ρ_s equal to -0.09. Therefore, the core detection is independent of the mass sensitivity range provided by the

observations. Figure 11 also shows that more massive clumps tend to fragment into more cores than less massive clumps. The group of six clumps with a below-average (<25) core count has an average clump mass of $\sim$770 $M_\odot$, while the group above the average has an average mass of 1560 $M_\odot$. Table 3 displays the position, peak flux, integrated flux, and radius for each individual core derived from dendrograms. The radius corresponds to half of the geometric mean between the deconvolved major and minor axes of the ellipse determined via dendrograms. All fluxes are primary beam corrected. Cores are named ALMA1, ALMA2, ALMA3... in order of descending peak intensity. Among all clumps, seven cores are located at the edge of the images ($\sim$20%– 30% power point) where flux measurements are more uncertain. They have been excluded from the forthcoming analyses in Section 5. However, their properties are still listed in Table 3.

Using the same set of input parameters for dendrograms in the 12 m-only images, a total of 242 cores were detected (20%
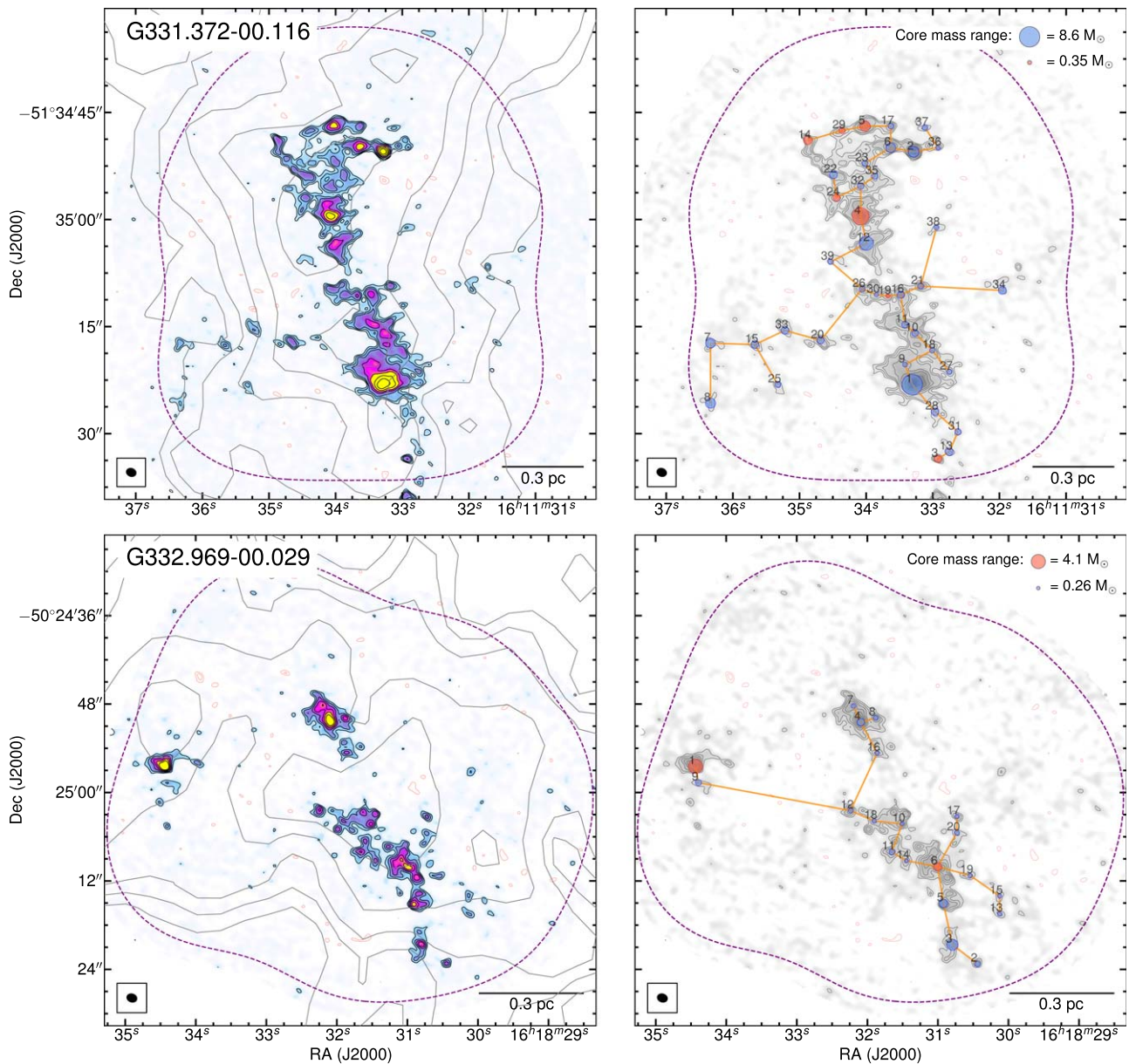
Figure 7. Same as in Figure 5, except for ALMA contour levels of −4, −3, 3, 4, 5, 7, 9, 12, and 16 × σ, with σ = 0.083 mJy beam^{-1}, for G331.372−00.116 (1″2 angular resolution); and −4, −3, 3, 4, 5, 6, 7, and 8 × σ, with σ = 0.080 mJy beam^{-1}, for G332.969−00.029 (1″2 angular resolution).

less than in the combined images). By adding the more extended flux recovered by the 7 m array, dust emission in the combined images increases signal-to-noise ratios above the 3.5σ threshold, allowing the detection of more cores. On average, cores detected in the combined images have higher integrated fluxes by a factor of 1.6 (with ∼75% of integrated fluxes increasing by a factor lower than 2). The inclusion of the 7 m array, with its maximum recoverable scale of ∼19″ is thus key to recover the flux from 1″ to 2″ cores. The cores sizes are much smaller (≲10%) than the maximum recoverable scale achieved in our observations, and only the diffuse, lower density intraclump emission is filtered out.

4.3. Evolutionary Stage of the Cores

Because the clumps in this study have neither emission detected at *Spitzer* wavelengths nor 70 μm emission from *Herschel*, all detected ALMA cores would be prestellar

candidates if we had no molecular line information at high angular resolution. Therefore, the evolutionary stage of the cores was assessed by systematically searching for molecular outflows and/or "warm core" line emission.

In 52 (17%) cores, molecular outflows were evident in the CO, SiO, and/or H_2CO lines (S. Li et al. 2019, in preparation). If outflows were detected in any of these tracers, the core was classified as protostellar. In this work, we refer to those molecular transitions with upper energy levels (E_u) larger than 22 K (defined by the E_u of the observed deuterated molecules), which are temperatures lower than those from typical "hot core" tracers (≳100 K), as "warm core" tracers. Cores with "warm core" line emission would be in an evolutionary stage prior to the "hot core" phase typically found in high-mass star formation. Therefore, if an ALMA core is associated with any of the two H_2CO warm transitions $J = 3_{2,2}-2_{2,1}$ ($E_u/k = 68.09$ K) and $J = 3_{2,1}-2_{2,0}$ ($E_u/k = 68.11$ K), or the CH_3OH $J_k = 4_{2,2}-3_{1,2}$ ($E_u/k = 45.46$ K) line, it was classified as
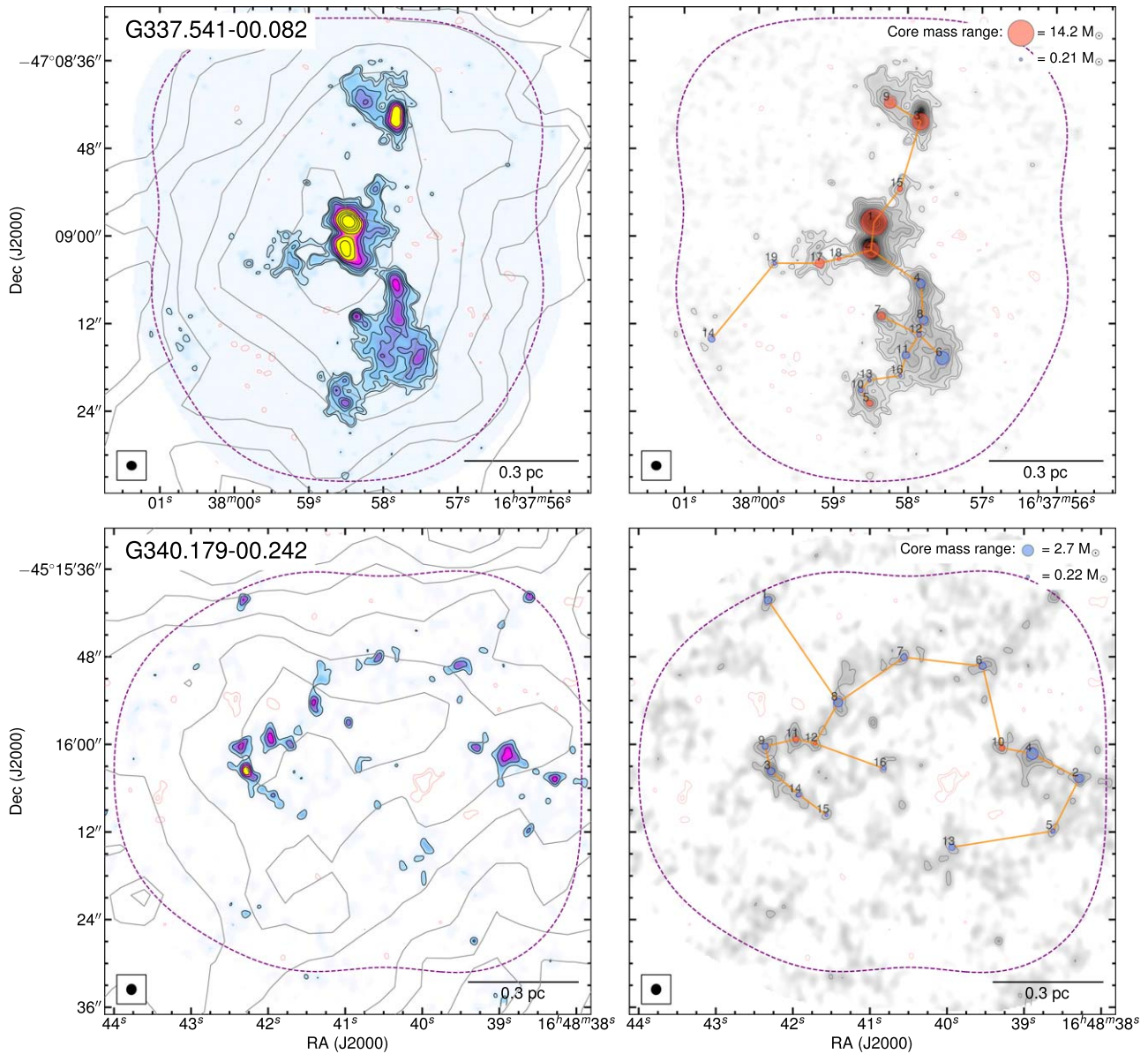
Figure 8. Same as in Figure 5, except for ALMA contour levels of -4, -3, 3, 4, 6, 8, 10, 14, 20, 30, 45, and $75 \times \sigma$, with $\sigma = 0.068$ mJy beam^{-1}, for G337.541–00.082 ($1''2$ angular resolution); and -4, -3, 3, 4, 5, and $6 \times \sigma$, with $\sigma = 0.094$ mJy beam^{-1}, for G340.179–00.242 ($1''3$ angular resolution).

protostellar (total of 62 cores, 21% of the whole sample). We note, however, that these transitions with high E_u/k could be subthermally excited and not really tracing star formation activity. Therefore, adopting their detection as a star formation indicator works as a strict limit that contributes to obtaining a pristine prestellar core sample. The 26 (9%) cores with both outflow and warm core lines are presumably more evolved. Cores with an absence of both molecular outflow and warm core tracers were categorized as prestellar. From the total of 301 cores, 213 (71%) are classified as prestellar, while 88 (29%) as protostellar. Table 3 includes a description for each individual core: if molecular outflows and warm core tracers are detected, or if the core is prestellar. In the core classification column (Table 3), a 0 is given for prestellar cores, while for the protostellar cores a 1 is given when molecular outflow emission alone is detected, a 2 when warm core line emission is detected, and a 3 when both protostellar indicators are detected (which would correspond to the most evolved cores in the sample).

Excluding the cores located at the edges, for the discussion in Section 5, we have 294 cores in total, with 210 (71%) prestellar candidates.

Based on this classification scheme, half of the clump sample shows evidence for some star formation activity, with <20% of cores having signs of star formation. Among them, only one clump (G340.222–00.167) seems completely prestellar. Considering that G340.222–00.167 is the most compact IRDC in the sample, this may indicate that G340.222–00.167 is young and maybe is still accreting mass to become a larger more massive IRDC. The most evolved clumps are G014.492–00.139 and G337.541–00.082, with $\gtrsim$50% of cores classified as protostellar. We therefore suggest that most of 70 μm dark clumps indeed have nascent, but deeply embedded, star formation activity. However, this star formation activity is, at the current evolutionary stage, apparently only from low-mass protostars that may become high mass in the future, as discussed in the following section.
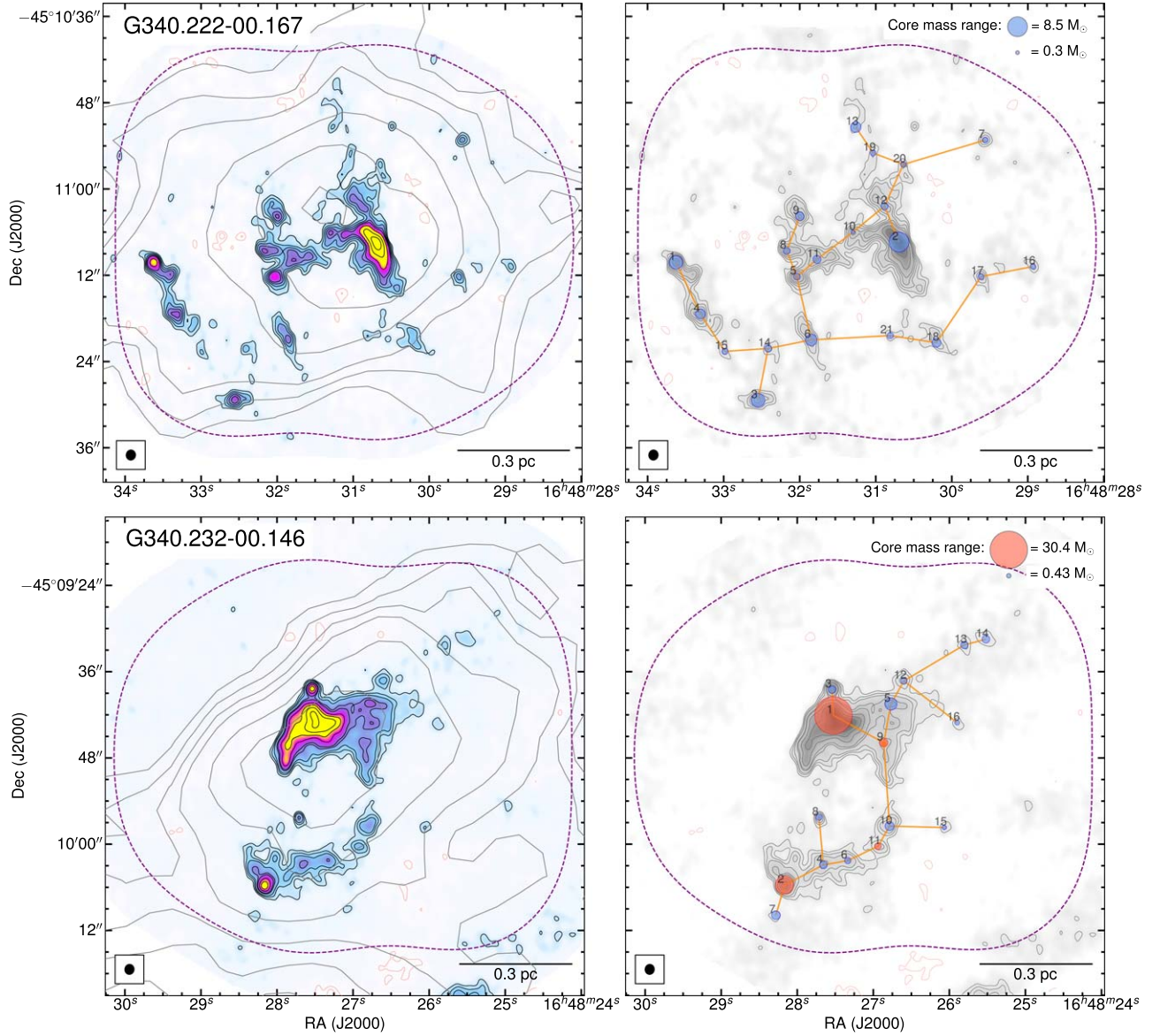
Figure 9. Same as in Figure 5, except for ALMA contour levels of -4, -3, 3, 4, 5, 6, 7, 10, 14, and $18 \times \sigma$, with $\sigma = 0.112$ mJy beam^{-1}, for G340.222–00.167 ($1\overset{''}{.}3$ angular resolution); and -4, -3, 3, 4, 5, 7, 8, 11, 14, 18, and $23 \times \sigma$, with $\sigma = 0.139$ mJy beam^{-1}, for G340.232–00.146 ($1\overset{''}{.}3$ angular resolution).

5. Discussion

5.1. Core Physical Properties

The mass of the cores was computed assuming optically thin dust continuum emission as follows:

$$M_{\mathrm{core}} = \mathbb{R} \, \frac{F_\nu D^2}{\kappa_\nu B_\nu(T)}, \qquad (1)$$

where F_ν is the measured integrated source flux, $\mathbb{R}$ is the gas-to-dust mass ratio, D is the distance to the source, κ_ν is the dust opacity per gram of dust, and B_ν is the Planck function at the dust temperature T. A value of $0.9 \, \mathrm{cm}^2 \, \mathrm{g}^{-1}$ is adopted for $\kappa_{1.3\mathrm{mm}}$, which corresponds to the opacity of dust grains with thin ice mantles at gas densities of $10^6 \, \mathrm{cm}^{-3}$ (Ossenkopf & Henning 1994). In the absence of dust temperature measurements at high angular resolution ($\sim 1''$), we have adopted the clump's dust temperature derived by Guzmán et al. (2015) using *Herschel* and APEX telescopes. Nevertheless, given the

early evolutionary stage of the clumps and the lack of hot cores, it is expected that the dust temperature throughout each cluster member does not strongly vary. A gas-to-dust mass ratio of 100 was assumed in this work. The number density, $n(\mathrm{H}_2)$, was calculated by assuming a spherical core and using the molecular weight per hydrogen molecule (μ_{H_2}) of 2.8. Masses, number densities, surface densities ($\Sigma = M_{\mathrm{core}}/(\pi r^2)$), and peak column densities ($N_{\mathrm{peak}}(\mathrm{H}_2)$) for all cores are listed in Table 4. The average core parameters for each clump are summarized in Table 5.

In spite of dust emission being the most reliable method for mass determination of star-forming cores, there are still several sources of uncertainty. Sanhueza et al. (2017) searched in the literature for possible values of $\mathbb{R}$ and κ_ν, finding the extreme possible values. Assuming the possible values are distributed in a uniform way between the extreme values, the standard deviation can be estimated (see details in Sanhueza et al. 2017). For $\mathbb{R}$, $1\sigma = 23$ corresponds to 23% of uncertainty of the
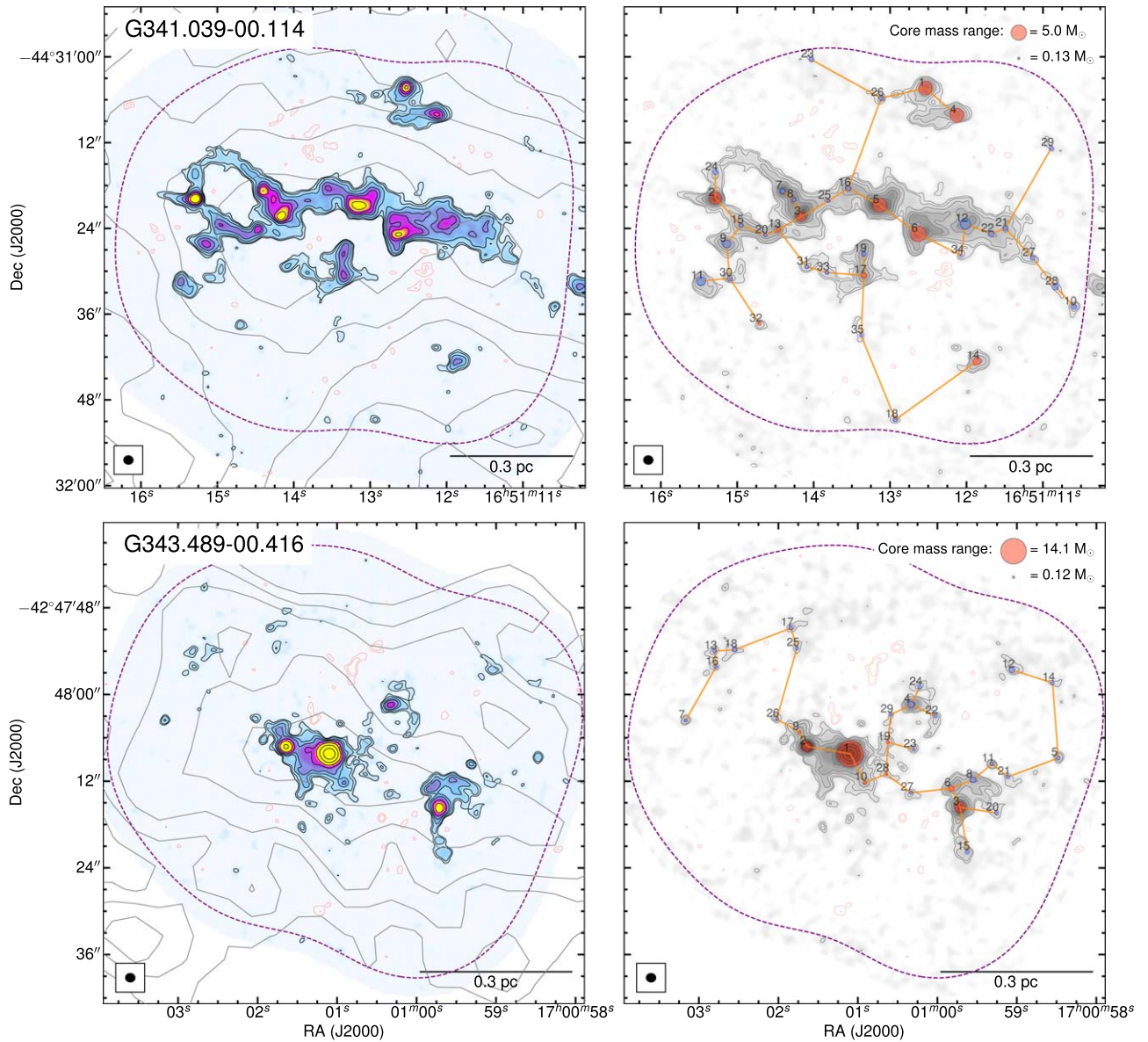
Figure 10. Same as in Figure 5, except for ALMA contour levels of $-4, -3, 3, 4, 6, 9, 12, 16,$ and $22 \times \sigma$, with $\sigma = 0.070$ mJy beam^{-1}, for G341.039–00.114 (1.″2 angular resolution); and $-4, -3, 3, 4, 6, 8, 12, 20, 40,$ and $100 \times \sigma$, with $\sigma = 0.068$ mJy beam^{-1}, for G343.489–00.416 (1.″2 angular resolution).

adopted value of 100. For κ_ν, $1\sigma = 0.25$ cm^2 g^{-1}, which corresponds to a 28% uncertainty in the adopted value of 0.9 cm^2 g^{-1}. Both $\mathbb{R}$ and κ_ν combined add an "intrinsic" uncertainty of 32% to the mass determination. Considering an absolute flux uncertainty of 10% for ALMA observations in band 6,[18] a dust temperature uncertainty <20%, and a distance uncertainty of ~10%, we estimate mass, number density, and surface density uncertainties of ~50%.

Figure 12 shows the core masses for each clump. Core masses range from 0.12 to 30.4 $M_\odot$, and eight cores have masses larger than 10 $M_\odot$. There is no correlation between the clump mass and the maximum core mass, with a Spearman's rank correlation coefficient, ρ_s, of 0.08. Therefore, at the earliest stages of fragmentation traced in the present study, there is no preference for more massive clumps to form the most massive cores. In Figure 12, the most massive prestellar

core in each clump is marked with a black cross. In four clumps, the most massive core is a prestellar core.

Figure 13 shows the distribution of core sizes, peak column densities, surfaces densities, and volume densities as a function of the core mass. The purpose of these plots is to show the distribution of the core properties at the earliest stage of high-mass star formation. The radii strongly correlate with mass, ρ_s equal to 0.71, and the correlation persists for individual clumps (see Figure 18 in Appendix B). We refrain from calculating correlation factors to other physical properties due to their intrinsic correlation with physical quantities (e.g., flux, mass, distance). Most peak column densities (~80%) are between 2×10^{22} and 10^{23} cm^{-2}. The bulk of cores (~90%) have surface densities between 0.1 and 1 g cm^{-2}. A non-negligible number of 31 cores (~10%) have Σ values larger than 1 g cm^{-2}. This value has been suggested by Krumholz & McKee (2008) to be the minimum necessary (but not sufficient) to halt fragmentation and allow the formation of high-mass stars. Volume densities are rather high, with more than 50%

---

[18] Absolute flux uncertainty quoted for band 6 in the ALMA proposal guide.

Table 3
Core Parameters Obtained from Dendrograms

IRDC Clump	Core Name	Position α(J2000)	Position δ(J2000)	Peak Flux (mJy beam^{-1})	Integrated Flux (mJy)	Radius ($''$)	Core Classification[a]	Notes[b]
G010.991−00.082	ALMA1	18:10:6.72	−19:27:46.5	2.70	12.63	1.35	3	0
G010.991−00.082	ALMA2	18:10:6.36	−19:28:13.8	2.33	2.80	0.50	3	0
G010.991−00.082	ALMA3	18:10:7.35	−19:28:2.6	2.27	4.91	0.71	1	0
G010.991−00.082	ALMA4	18:10:6.94	−19:27:35.9	1.90	4.04	0.77	3	0
G010.991−00.082	ALMA5	18:10:7.82	−19:28:8.7	1.40	4.33	0.83	0	0

Notes.
[a] Core classification ranges from 0 to 3, meaning: 0 = prestellar candidate, 1 = only molecular outflow emission is detected, 2 = only warm core line emission is detected, and 3 = both protostellar indicators are detected.
[b] Cores indicated with 0 are used in the analysis in Section 5, while cores indicated with 1 are not used because they are located near the edge of the images (seven cores; properties are still given here for completeness).

(This table is available in its entirety in machine-readable form.)

Table 4
Calculated Properties for the Whole Core Sample

IRDC Clump	Core Name	Mass ($M_\odot$)	Radius (au)	$n(H_2)$ ($\times 10^6$ cm^{-3})	Σ (g cm^{-2})	$N_{peak}(H_2)$ ($\times 10^{23}$ cm^{-2})
G010.991−00.082	ALMA1	8.09	5000	2.0	0.91	1.90
G010.991−00.082	ALMA2	1.79	1840	8.7	1.49	1.63
G010.991−00.082	ALMA3	3.15	2620	5.3	1.29	1.59
G010.991−00.082	ALMA4	2.59	2870	3.3	0.89	1.33
G010.991−00.082	ALMA5	2.77	3080	2.9	0.82	0.98

Note. $n(H_2)$, Σ, and $N(H_2)$ correspond to number density, surface density, and peak column density, respectively.

(This table is available in its entirety in machine-readable form.)

having values larger than 10^6 cm^{-3}. The effect of assuming 30 K for protostellar cores, instead of the clump temperatures that are about a factor of 2 lower, can be seen in Appendix B, Figure 19.

5.2. Low-mass Core Population

Notably, a large population of low-mass cores ($<1\,M_\odot$) is detected, contrary to what has been observed with ALMA, at similar mass sensitivity in more-evolved star-forming regions (e.g., IRDC G28.34+0.06, Zhang et al. 2015; G11.92–0.61, Cyganowski et al. 2017). From the total of 294 cores, 159 cores (54%) have masses $<1\,M_\odot$. We find that 56% of the core population with masses $<1\,M_\odot$ (55% for $<2\,M_\odot$) are located outside a circle of 25$''$2 diameter (equivalent to the primary beam of the ALMA 12 m antenna) centered on the ATLASGAL position. With single-pointing observation, Zhang et al. (2015) found a lack of a widespread low-mass protostellar population and suggest that low-mass protostars form after high-mass stars. However, Kong et al. (2018a) observed the same IRDC on a large mosaic revealing cores previously undetected, which may suggest that mapping a larger area plays an important role in detecting a low-mass population of cores. This may be the case in the work by Cyganowski et al. (2017), which indeed found a widespread population of low-mass cores ($\sim$1–2 $M_\odot$). Based on different approaches, Foster et al. (2014) and later Pillai et al. (2019) suggest that low-mass stars may form earlier or coevally with high-mass stars. Foster et al. (2014) observed an IRDC using deep near-infrared observations and discovered a distributed population of low-mass protostars. Part of the area is covered by ALMA (Sakai et al. 2013, 2015, 2018; Yanagida et al. 2014) and most of
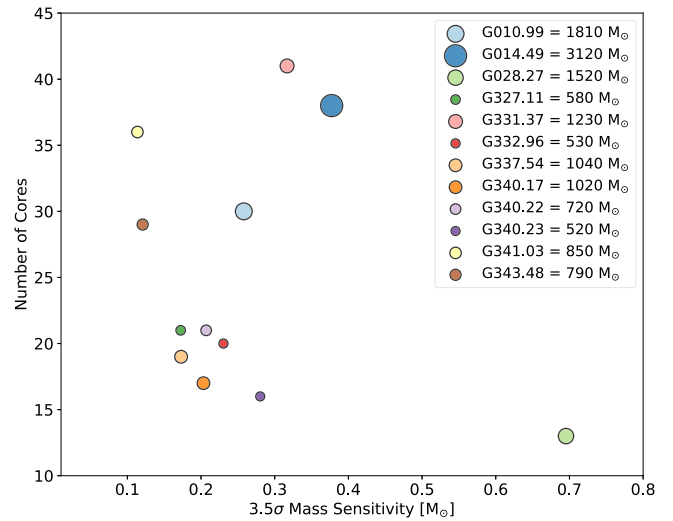

Figure 11. Number of cores detected by clump against the 3.5σ mass sensitivity. The value of sigma corresponds to the point-source sensitivity at the clump's temperature. The size of the circles depends on the mass of the clump as shown on the label. Core detection is independent of mass sensitivity, ignoring the outlier at the bottom, right. Massive clumps tend to fragment more than less massive clumps.

the low-mass protostars revealed in near-IR have no counterpart in 1.3 mm dust continuum emission. The low-mass protostars may presumably be a relatively older population with no significant envelope to be detected by ALMA. Using CO $J = 2$–1 outflow emission, Pillai et al. (2019) inferred that low-mass protostars

Table 5
Overall Properties Per Clump of the Embedded ALMA Cores

IRDC Clump	1σ Mass Sensitivity ($M_{\odot}$)	Number of Cores	Core Mass		Mean					Number of Pre-/Protostellar Cores
			Min. ($M_{\odot}$)	Max. ($M_{\odot}$)	Mass ($M_{\odot}$)	Radius (au)	$n(H_2)$ ($\times 10^6$ cm^{-3})	Σ (g cm^{-2})	$N_{peak}(H_2)$ ($\times 10^{22}$ cm^{-2})	
G010.991–00.082	0.074	28	0.31	8.1	1.35	2370	2.9	0.57	6.80	18/10
G014.492–00.139	0.108	37	0.62	20.7	3.30	2290	8.9	1.63	16.4	12/25
G028.273–00.167	0.199	13	1.46	10.9	4.93	4810	1.5	0.57	6.48	11/2
G327.116–00.294	0.049	21	0.19	10.6	1.54	2940	1.6	0.39	5.07	17/4
G331.372–00.116	0.091	39	0.35	8.6	1.40	3460	1.0	0.29	3.13	32/7
G332.969–00.029	0.066	20	0.26	4.1	0.87	2670	1.2	0.28	3.12	18/2
G337.541–00.082	0.049	19	0.21	14.2	2.29	2840	2.7	0.67	7.61	10/9
G340.179–00.242	0.058	16	0.22	2.7	0.91	3710	0.6	0.18	2.10	13/3
G340.222–00.167	0.059	21	0.30	8.5	1.79	4100	0.8	0.27	3.22	21/0
G340.232–00.146	0.080	16	0.43	30.4	3.44	3510	1.6	0.46	5.02	12/4
G341.039–00.114	0.032	35	0.13	5.0	1.09	2520	1.9	0.39	4.34	25/10
G343.489–00.416	0.035	29	0.12	14.1	0.92	1810	2.9	0.51	7.33	21/8

Note. Total of 294 cores with 210 prestellar candidates. $n(H_2)$, Σ, and $N(H_2)$ correspond to number density, surface density, and peak column density, respectively.
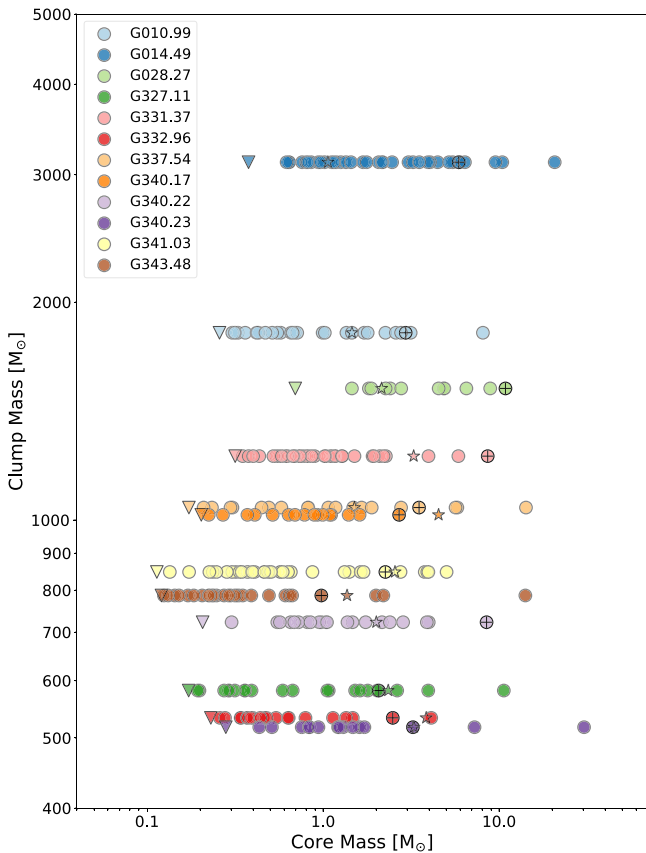

Figure 12. Clump masses against the core masses. Triangles indicate the 3.5σ level above which cores are defined. Stars show the value of the Jeans mass of each clump. Encircled plus signs indicate the most massive prestellar core in each clump. No correlation between the clump mass and the maximum core mass is found. A large population of low-mass cores ($<1\,M_{\odot}$) is detected. The range of core masses is well explained by thermal Jeans fragmentation, without the need to invoke turbulent Jeans fragmentation.

($<1\,M_{\odot}$). This suggests that the seeds of high-mass stars form and evolve together with the seeds of low-mass stars.

5.3. Lack of High-mass Prestellar Cores

Table 6 presents a list of cores with masses larger than $10\,M_{\odot}$. When a clump has no cores with masses larger than $10\,M_{\odot}$, the most massive core is listed. Half of clumps have cores with masses above $10\,M_{\odot}$, and two of them, G014.492–00.139 and G028.273–00.167, have two. Except for the two cores in G028.273–00.167, all cores with masses larger than $10\,M_{\odot}$ are protostellar. All cores in Table 6 are resolved or barely resolved. All eight cores with masses larger than $10\,M_{\odot}$ have surface densities $\gtrsim 0.8\,\mathrm{g\,cm^{-2}}$, similar to values found in the most massive cores embedded in more-evolved IRDCs (e.g., Tan et al. 2013; Kong et al. 2017). Of these eight cores, four of them have extreme volume densities of a few times $10^7\,\mathrm{cm^{-3}}$ and peak column densities higher than $5 \times 10^{23}\,\mathrm{cm^{-2}}$.

Following the discussion from Sanhueza et al. (2017), the definition of a bona fide "high-mass prestellar core" is rather vague. Longmore et al. (2011) suggest that in order to form an O-type star through the direct collapse of a core, the core should have of the order of $100\,M_{\odot}$. This is consistent with the simulations of Krumholz et al. (2007), in which a high-mass star of $9\,M_{\odot}$ is formed from a turbulent, virialized core of $100\,M_{\odot}$. Tan et al. (2014) suggest that a high-mass prestellar core should contain ~ 100 core Jeans masses. Another important piece of information in the definition of a high-mass prestellar core is that $\sim 80\%$ of high-mass stars are found in binary systems (Kouwenhoven et al. 2005; Chini et al. 2012) and that the majority of the high-mass systems contain pairs of similar mass. Combining all this information, it seems clear that a high-mass prestellar core should have several tens of solar masses. In this work, we define a high-mass core as a core with a mass larger than $\sim 30\,M_{\odot}$. This definition is consistent with the star formation efficiency[19] of 30% derived by Alves et al. (2007) in the Pipe dark cloud (also tentatively determined

formed before or coevally with high-mass cores. In our work, which samples a greater number of clumps, covers a lager mosaic area per clump, and recovers extended flux using the 7 m array, we find a large, widespread population of low-mass cores

---

[19] We note, however, that in clump-feed star formation scenarios, star formation efficiencies are larger than 100% for cores forming high-mass stars. This is because cores start with masses lower than $8\,M_{\odot}$ and end by forming a high-mass star ($>8\,M_{\odot}$).
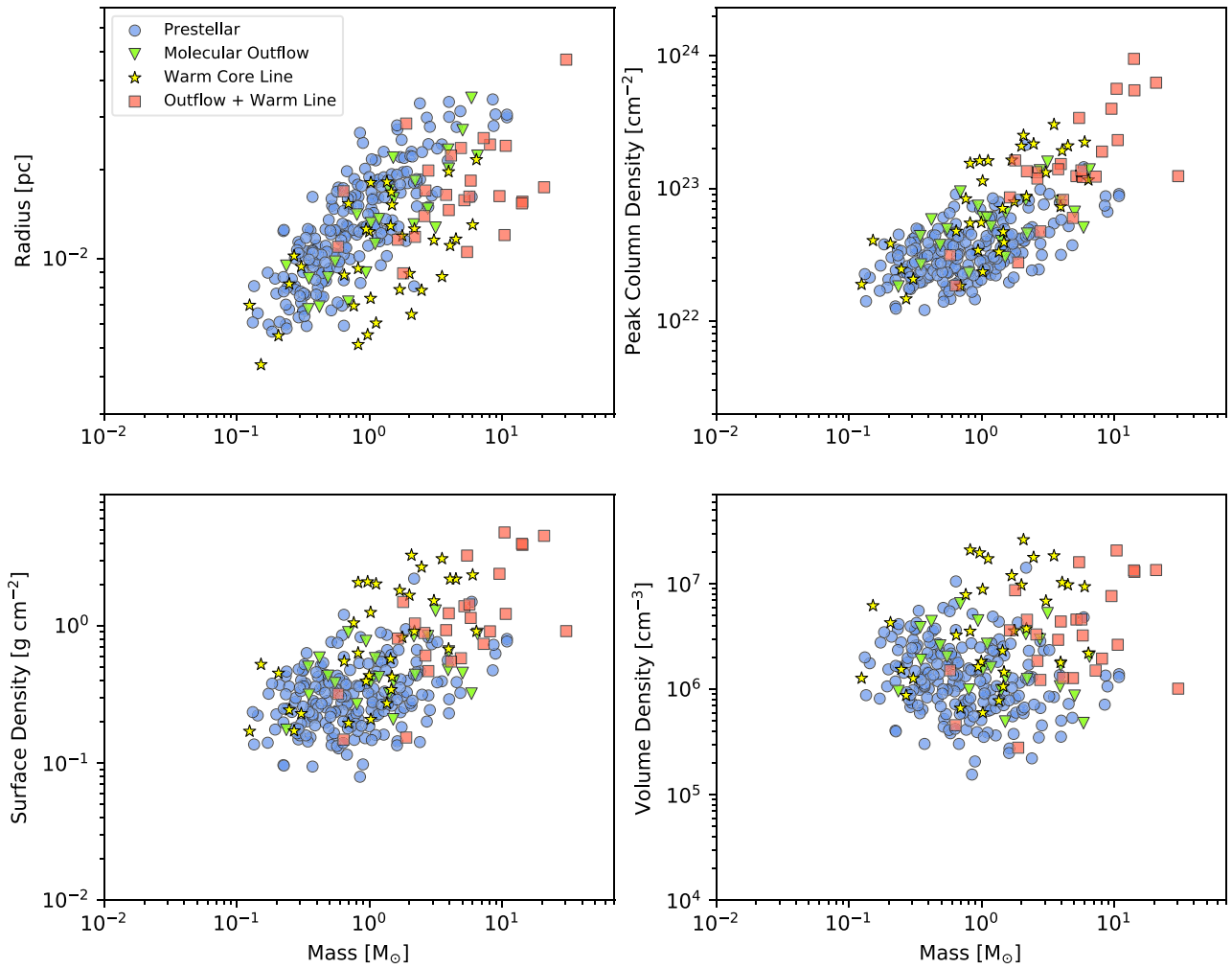
Figure 13. Radius, peak column, surface density, and volume density of cores against the core mass color-coded by protostellar activity (prestellar, molecular outflow only, warm core line only, and both protostellar indicators; see Section 4.3). The purpose of these scatter plots is to show the distribution of core properties.

in the Cygnus X complex by Bontemps et al. 2010), assuming that the IMF is a direct product of the CMF as stated for the turbulent core accretion model; see, e.g., Tan et al. (2014). The adopted value of 30 $M_\odot$ is also consistent with the core Jeans mass determined for the most massive prestellar cores detected in this sample. The prestellar cores with masses of ∼11 $M_\odot$ (density ∼1.4 × 10⁶ cm⁻³) have a core Jeans mass of ∼0.3 $M_\odot$. Therefore, the most massive prestellar cores contain only ∼40 core Jeans masses. In order to reach 100 core Jeans masses (Tan et al. 2014), these cores would need instead a mass of 30 $M_\odot$ (maintaining the same density).

In the sample observed in the pilot survey, there are no high-mass prestellar cores. Remarkably, high-mass prestellar cores are inexistent even when adopting higher star formation efficiencies of 40%–50%. The most massive core (30.4 $M_\odot$), located in G340.232−00.146, shows evidence of protostellar activity, based on warm core line emission and molecular outflows. However, this core is rather large (radius of ∼10,000 au) and after visual inspection of the dendrogram leaf structure, it seems likely that higher angular resolution observations will reveal a more fragmented structure with smaller condensations.

5.4. Fragmentation

If clump fragmentation is governed by thermal Jeans instabilities, the initially homogeneous gas fragments into smaller objects defined by the Jeans length (λ_J) and the Jeans mass (M_J):

$$\lambda_J = \sigma_{\rm th}\left(\frac{\pi}{G\rho}\right)^{1/2}, \qquad (2)$$

and

$$M_J = \frac{4\pi\rho}{3}\left(\frac{\lambda_J}{2}\right)^3 = \frac{\pi^{5/2}}{6}\frac{\sigma_{\rm th}^3}{\sqrt{G^3\rho}}, \qquad (3)$$

where ρ is the mass density and $\sigma_{\rm th}$ is the thermal velocity dispersion (or isothermal sound speed, c_s) given by

$$\sigma_{\rm th} = \left(\frac{k_{\rm B}T}{\mu m_{\rm H}}\right)^{1/2}. \qquad (4)$$

The thermal velocity dispersion is mostly dominated by H_2 and He, and it should be derived by using the mean molecular weight per free particle, $\mu = 2.37$. The mean Jeans length for

Table 6
Properties of Most Massive Cores

IRDC Clump	Core Name	Mass $(M_\odot)$	Mass/M_J	Radius (au)	$n(H_2)$ $(\times 10^6 \, \mathrm{cm}^{-3})$	Σ $(\mathrm{g \, cm}^{-2})$	$N_{\mathrm{peak}}(H_2)$ $(\times 10^{23} \, \mathrm{cm}^{-2})$	Core Classification
G010.991–00.082	ALMA1	8.1	5.5	5000	2.0	0.91	1.90	protostellar
G014.492–00.139	ALMA1	20.7	19.4	3590	13.5	4.52	6.29	protostellar
G014.492–00.139	ALMA2	10.4	9.8	2480	20.8	4.78	5.66	protostellar
G028.273–00.167	ALMA2	10.9	5.1	6180	1.4	0.80	0.91	prestellar
G028.273–00.167	ALMA3	10.9	5.1	6310	1.3	0.77	0.88	prestellar
G327.116–00.294	ALMA1	10.6	4.5	4950	2.6	1.22	2.32	protostellar
G331.372–00.116	ALMA1	8.6	2.6	5780	1.4	0.73	0.87	prestellar
G332.969–00.029	ALMA1	4.1	1.1	4600	1.3	0.55	0.82	protostellar
G337.541–00.082	ALMA1	14.2	9.4	3210	13.0	3.88	5.51	protostellar
G340.179–00.242	ALMA4	2.7	0.6	6160	0.3	0.20	0.25	prestellar
G340.222–00.167	ALMA2	8.5	4.2	7100	0.7	0.47	0.74	prestellar
G340.232–00.146	ALMA1	30.4	9.3	9670	1.0	0.91	1.24	protostellar
G341.039–00.114	ALMA6	5.0	2.0	5600	0.9	0.45	0.67	protostellar
G343.489–00.416	ALMA1	14.1	10.3	3170	13.4	3.95	9.52	protostellar

Note. This table includes all cores with masses larger than 10 $M_\odot$. When a clump has no core above 10 $M_\odot$, the most massive core is listed. M_J is the clump Jeans mass (see Table 7).
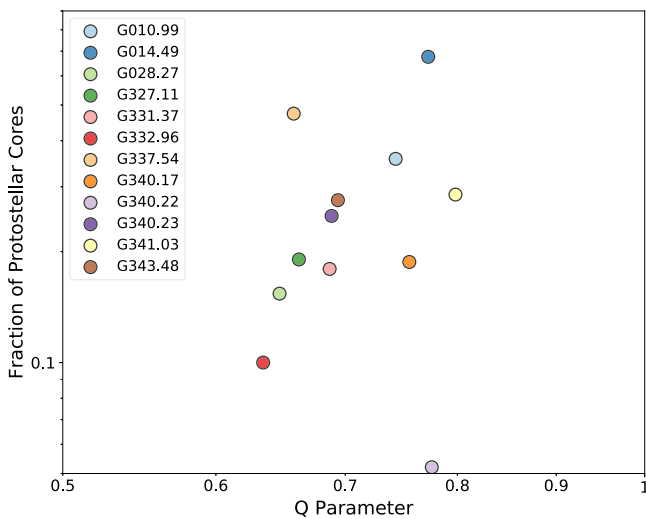

Figure 14. Spatial distribution of cores (characterized by the $\mathcal{Q}$ parameter) vs. the fraction of protostellar cores per clump, as a proxy of clump evolution. A weak correlation with a Spearman correlation coefficient $\rho_s = 0.28$ is measured. After excluding the "outlier" clump with no protostellar cores (G340.222–00.167), the correlation becomes stronger with $\rho_s = 0.59$. For display reasons in the log–log plot, we artificially assigned a protostellar fraction of 0.05 to G340.222–00.167.

all clumps is 0.14 pc, ranging from 0.06 to 0.24 pc. The mean Jeans mass is 2.5 $M_\odot$, ranging from 1.1 to 4.5 $M_\odot$. If the fragmentation is driven by turbulence, the turbulent Jeans lengths and masses can be derived by replacing σ_{th} by the observed clump velocity dispersion listed in Table 1. The turbulent Jeans length (λ_{turb}) for the whole clump sample has a mean of 0.87 pc, ranging from 0.3 to 1.6 pc. The turbulent Jeans mass (M_{turb}) for all clumps has a mean of 950 $M_\odot$, ranging from 40 to 4710 $M_\odot$. Therefore, turbulent Jeans lengths and masses are at least 2.5 times and 16 times larger than the corresponding thermal ones (on average 7 and 440 times larger, respectively). Table 7 displays in column (1) the clump name, in column (2) the thermal velocity dispersion, in column (3) the

Jeans mass, in column (4) the Jeans length, in column (5) the turbulent Jeans mass, and in column (6) the turbulent Jeans length.

5.4.1. Jeans Length and Core Separation

To quantify core separations to compare with Jeans lengths, we used the MST method, first developed for astrophysical applications by Barrow et al. (1985). MST determines a set of straight lines connecting a set of points (cores in this case) that minimizes the sum of the lengths. More details on this method can be found, for example, applied to simulations in Wu et al. (2017) and to observations in Dib & Henning (2019).

Figures 5–10 display the MST for each clump, and Table 7 lists (column 7) the average minimum separation (L_{av}) between cores determined by MST for each clump. The mean L_{av} for all clumps is 0.11 pc, ranging from 0.07 to 0.17 pc. However, L_{av} is the measured separation projected on the sky and the real (unprojected) value is equal or longer. On average, the observed separation will be $2/\pi$ times smaller than the unprojected one.[20] We therefore divide L_{av} by this factor to obtain L_{avcorr} (Table 7, column 8). Given that L_{avcorr} is comparable to or slightly larger than the Jeans length by a factor 0.7 to 2, but consistent within the uncertainties, the clump fragmentation is governed by thermal Jeans fragmentation. Turbulent Jeans lengths are a factor of 2, up to 10, larger than L_{avcorr}. We therefore discard turbulent Jeans fragmentation as the controlling process of the early stages of high-mass star and cluster formation found in these IRDCs.

5.4.2. Jeans Mass

We find that $\sim$74% of cores have masses lower than the Jeans mass, further indicating that turbulence does not play an important role in the global fragmentation of IRDCs. A large

---

[20] The average value for cos i, with i the angle between the core separation and the observed projected separation, is given by

$$\frac{1}{\pi} \int_{-\frac{\pi}{2}}^{\frac{\pi}{2}} \cos(x) \, dx = \frac{2}{\pi}.$$

Table 7
Global Structure Parameters

IRDC Clump (1)	σ_{th} (km s^{-1}) (2)	M_J ($M_\odot$) (3)	λ_J (pc) (4)	M_{turb} ($M_\odot$) (5)	λ_{turb} (pc) (6)	L_{av} (pc) (7)	L_{avcorr} (pc) (8)	$\mathcal{Q}$ (9)
G010.991–00.082	0.20	1.5	0.09	350	0.57	0.08	0.12	0.74
G014.492–00.139	0.21	1.1	0.06	520	0.49	0.07	0.11	0.77
G028.273–00.167	0.20	2.2	0.13	130	0.53	0.17	0.27	0.65
G327.116–00.294	0.22	2.3	0.12	40	0.31	0.10	0.16	0.66
G331.372–00.116	0.22	3.3	0.18	650	1.03	0.11	0.18	0.69
G332.969–00.029	0.21	3.9	0.23	1180	1.55	0.10	0.16	0.63
G337.541–00.082	0.20	1.5	0.09	1430	0.93	0.10	0.15	0.66
G340.179–00.242	0.22	4.5	0.24	1370	1.63	0.16	0.25	0.76
G340.222–00.167	0.23	2.0	0.10	4710	1.34	0.13	0.20	0.78
G340.232–00.146	0.22	3.3	0.18	560	0.98	0.12	0.19	0.69
G341.039–00.114	0.22	2.6	0.13	210	0.59	0.10	0.16	0.80
G343.489–00.416	0.19	1.4	0.10	200	0.53	0.07	0.11	0.69

Note. Uncertainty ranges for the quantities above are σ_{th}, from 2% to 11%; M_J, from 25% to 45%; λ_J, from 24% to 27%; M_{turb}, from 25% to 36%; λ_{turb}, from 24% to 26%; L_{av} and L_{avcorr}, around 10%. $\mathcal{Q}$ is distance independent and has negligible uncertainties.

population of cores with masses $\lesssim M_J$ favors competitive accretion and global hierarchical collapse scenarios. The remaining 26% of cores have masses on average three times the Jeans mass (up to $19 \times M_J$). If these relatively massive cores remain as single objects at higher angular resolution observations, they would need additional support, by, for example turbulence and/or magnetic field, to avoid fragmentation. After accreting material from their surroundings, these super-Jeans cores are prime candidates to evolve into high-mass cores and form high-mass stars (see Table 6 for the most massive cores).

5.5. Spatial Core Distribution and Mass Segregation

5.5.1. Spatial Core Distribution

Considering that the IRDC clumps in this study represent the earliest stages of high-mass and cluster formation, the spatial distribution of cores gives a characteristic imprint of the early fragmentation. Some clumps, for example G014.492–00.139, show a more centrally concentrated core distribution, while others, like G327.116–00.294, have a more widespread core distribution.

To quantify the spatial distribution of cores, we follow the approach of Cartwright & Whitworth (2004) and define the $\mathcal{Q}$ parameter that can be used to distinguish between centrally peaked clusters of cores ($\mathcal{Q} > 0.8$) and hierarchical subclustering ($\mathcal{Q} < 0.8$). The $\mathcal{Q}$ parameter is defined as

$$\mathcal{Q} = \frac{\bar{m}}{\bar{s}}, \quad (5)$$

where $\bar{m}$ is the the normalized mean edge length of the MST, given by

$$\bar{m} = \sum_{i=1}^{N_c-1} \frac{L_i}{(N_c A)^{1/2}}, \quad (6)$$

where N_c is the number of cores, L_i is the length of each edge, and A is the cluster area, $A = \pi R_{cluster}^2$, with $R_{cluster}$ calculated as the distance from the mean position of all cores to the farthest core. $\bar{s}$ is the normalized correlation length, i.e., the

ratio of the mean core separation to the cluster radius, $R_{cluster}$:

$$\bar{s} = \frac{L_{av}}{R_{cluster}}. \quad (7)$$

Both $\bar{m}$ and $\bar{s}$ are independent of the number of cores in the cluster-forming clump (see further details in Cartwright & Whitworth 2004).

For $\mathcal{Q} > 0.8$, $\mathcal{Q}$ is correlated with centrally condensed spatial distributions with radial density profiles of the form $n(r) \propto r^{-\alpha}$ (with α between 0 and 3), while for $\mathcal{Q} < 0.8$, $\mathcal{Q}$ is associated with the fractal dimension, D (see Figure 5 in Cartwright & Whitworth 2004). A value of $\mathcal{Q} \simeq 0.8$ implies uniform density (i.e., $\alpha = 0$) and no subclustering ($D = 3$). The value of D ranges from 3 (no subclustering) to 1.5 (strong subclustering, $\mathcal{Q} \simeq 0.45$).

As cluster-forming clumps evolve over time, it may be expected that the primordial distribution of cores dissolves, due to dynamical relaxation to become radially concentrated. If this is the case, we may expect to see higher $\mathcal{Q}$ values toward more-evolved clumps (those containing a larger fraction of proto-stellar cores). Table 7 (column 9) summarizes the $\mathcal{Q}$ parameters measured toward each clump. The narrow range in $\mathcal{Q}$ values (0.63–0.80) may indicate that the evolutionary stage of the clumps is similar; indeed, the embedded protostars have not significantly affected the clumps (all are 70 μm dark). Never-theless, we still find a weak correlation between the $\mathcal{Q}$ parameter and the fraction of protostellar cores in each clump (Figure 14), with a Spearman correlation coefficient $\rho_s = 0.28$. The correlation becomes stronger if we remove the "outlier" clump with no protostellar cores (G340.222–00.167), with $\rho_s = 0.59$. Those clumps with $\mathcal{Q} \sim 0.8$ are consistent with spatial core distributions of uniform density ($\alpha = 0$). However, the whole sample shows $\mathcal{Q} \lesssim 0.8$ (and thus $D \lesssim 3$), indicating that the initial fragmentation in IRDCs favors (moderate) hierarchical subclustering over centrally peaked clustering.

5.5.2. Mass Segregation

Mass segregation (as defined by, e.g., Allison et al. 2009; Parker & Goodwin 2015) refers to a different distribution (more concentrated) of massive objects with respect to lower mass objects than that expected by random chance. Mass

segregation is observed in evolved clusters where it is believed to be produced by two-body relaxation (dynamical mass segregation), with some exceptions as described in Bonnell & Davies (1998). Primordial mass segregation is especially important because it has been predicted as a natural outcome of competitive accretion models (Bonnell & Davies 1998; Bonnell & Bate 2006), in which the cores located at the center of the cluster accrete enough material to become massive and form high-mass stars. We note, however, that cluster formation simulations that are in agreement with the turbulent core accretion theory also find primordial mass segregation (Myers et al. 2014). Considering (i) the early evolutionary stage of the IRDC clumps observed in this study, all are IR dark with no signs of disruption from high-mass stars, and (ii) the large area mosaicked per clump that should cover most of the cluster members, this is an ideal sample in which to search for primordial mass segregation.

To quantify mass segregation, we use the mass segregation ratio (MSR), Λ_{MSR}, as defined by Allison et al. (2009) and Γ_{MSR} as defined by Olczak et al. (2011), both based on the MST method. The first method (Λ_{MSR}) compares the MSTs of random subsets of cluster members with the MST of the same number of most massive members. The value of Λ_{MSR} is given by

$$\Lambda_{\mathrm{MSR}}(N_{\mathrm{MST}}) = \frac{\langle l_{\mathrm{random}} \rangle}{l_{\mathrm{massive}}} \pm \frac{\sigma_{\mathrm{random}}}{l_{\mathrm{massive}}}, \qquad (8)$$

where $\langle l_{\mathrm{random}} \rangle$ is the average MST length of sets of N_{MST} random cores and l_{massive} is the MST length of the N_{MST} most massive cores. A total of 1000 sets of random N_{MST} cores were used to derive the average MST length. σ_{random} is the standard deviation associated with $\langle l_{\mathrm{random}} \rangle$, i.e., the standard deviation of the 1000 sets of l_{random}. If the MST length of the most massive cores is shorter than the mean MST length of the random cores, the massive cores have a different, more concentrated distribution. Therefore, $\Lambda_{\mathrm{MSR}} \approx 1$ means massive cores are distributed in the same way than other cores (no mass segregation), $\Lambda_{\mathrm{MSR}} > 1$ indicates massive cores are concentrated (mass segregation), and $\Lambda_{\mathrm{MSR}} < 1$ implies more massive cores are spread out compared to other cores (inverse-mass segregation). The second method (Γ_{MSR}) uses an approach analogous with the difference of the geometric mean of the segments forming the MST length being used (instead of the arithmetic mean). The value of Γ_{MSR} is given by

$$\Gamma_{MSR}(N_{\mathrm{MST}}) = \frac{\gamma_{\mathrm{random}}}{\gamma_{\mathrm{massive}}} (d\gamma_{\mathrm{random}})^{\pm 1}, \qquad (9)$$

where γ_{random} is the geometric mean of the MST segments for the N_{MST} random cores (1000 sets), $\gamma_{\mathrm{massive}}$ is the MST of the N_{MST} more massive cores, and $d\gamma_{\mathrm{random}}$ is the geometric standard deviation given by (Olczak et al. 2011)

$$d\gamma = \exp\left(\sqrt{\frac{\sum_{i=1}^{n} (\ln L_i - \ln \gamma_{\mathrm{MST}})^2}{n}} \right), \qquad (10)$$

where L_i are the n MST lengths. The values obtained for Γ_{MSR} are interpreted in the same way as Λ_{MSR}, and according to Olczak et al. (2011), Γ_{MSR} would be more sensitive to finding weak mass segregation.
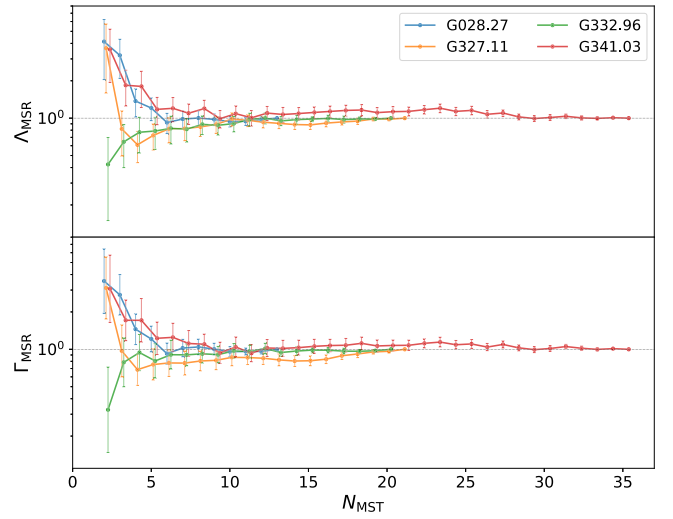
Figure 15. Mass segregation ratios (Λ_{MSR} and Γ_{MSR}) for different numbers of N_{MST} cores for the four clumps with ratios having marginal departures from unity. For instance, if $N_{\mathrm{MST}} = 3$, Λ_{MSR} and Γ_{MSR} are calculated 1000 times from the ratio of the MST length derived from three random cores in the cluster and the MST length derived for the three most massive cores. A $\Lambda_{\mathrm{MSR}} \approx 1$ (and $\Gamma_{\mathrm{MSR}} \approx 1$) implies no mass segregation.

There is no mass segregation for eight clumps and only marginal departure from unity in four clumps. Figure 15 shows the derived Λ_{MSR} and Γ_{MSR} parameters in these four clumps at several N_{MST} values. For $N_{\mathrm{MST}} = 2$ and $N_{\mathrm{MST}} = 3$, there are three clumps with MSR values $\gtrsim 3$ (weak mass segregation) and one with ~ 0.4–0.5 (weak inverse-mass segregation). Although the MSR values have a significance larger than 1σ above or below unity, the results are not robust considering the low number of cores (two or three). A different assumption for dust temperature on individual cores can modify the mass and completely change the output from an MSR with small N_{MST}. We tested the effect of changing the temperature for the protostellar cores to 30 K and verified that the results are consistent with using the lower clump temperature. The overall conclusion is that there is no significant evidence of primordial mass segregation, i.e., more massive cores are distributed in the same way as other cores in this IRDC sample.

5.6. Core Mass Function

The IMF is an empirical function that describes the initial distribution of masses of a stellar population, and it is believed to be the result of star formation. The IMF has a shape similar to a log normal with a peak below 1 $M_{\odot}$ and a power-law tail at the high-mass end of the form

$$\frac{dN}{d\log M} \propto M^{-\alpha}, \qquad (11)$$

with an index $\alpha = 1.35$ (Salpeter 1955) that is considered to be universal (e.g., Bastian et al. 2010; Kroupa et al. 2013). In order to understand the origin of the universal IMF, the histogram of core masses (or CMF) has been constructed mostly for nearby, low-mass star-forming regions. In this case, the CMF resembles the IMF in shape, but apparently shifted to higher masses by an efficiency factor (e.g., Alves et al. 2007; André et al. 2010; Könyves et al. 2015). This similarity has been interpreted as the IMF being for the most part determined

by the fragmentation process of molecular clouds. On the other hand, the few, more distant, high-mass star-forming regions observed with ALMA so far point to a more dynamical picture. Motte et al. (2018) found in the young massive cluster W43-MM1 a power-law index $\alpha = 0.90 \pm 0.06$, much shallower than the Salpeter IMF. Their results can be interpreted as the CMF evolving over time from a shallower distribution to the universal IMF, likely producing low-mass objects continuously over the formation of the cluster while the massive objects were mostly formed early on. Cheng et al. (2018) derived in the later-stage protocluster G286.21+0.17 located in Carina a power-law index of 1.24 ± 0.17, slightly shallower but consistent with Salpeter within the uncertainties. More recently, in a combined CMF for clumps in seven IRDCs, Liu et al. (2018a) found a power-law index of 0.86 ± 0.11. We note that these IRDCs, originally selected from Rathborne et al. (2006) by Butler & Tan (2009), are in a more advanced evolutionary stage than those observed in this work, containing several embedded clumps with protostellar activity inferred from *Spitzer* images (see images in Chambers et al. 2009 and an updated classification in Sanhueza et al. 2012).

The IRDC clumps in ASHES are IR dark from 3.6 to 70 μm in *Spitzer* and *Herschel* images (see Figures 1–4) ,and the ALMA observations reveal that only 29% of the embedded cores have star formation activity. With a large population of prestellar core candidates, the CMF would likely represent a snapshot of the initial core mass distribution produced in massive clumps that will form high-mass stars. Figure 16 shows the CMF for the prestellar core population (in blue; 210 cores) and, as a reference, the whole core population (in black; 294 cores). The power-law index for the prestellar core population is $\alpha = 1.17 \pm 0.10$ (blue dashed line), which is slightly, but significantly, shallower than Salpeter ($\alpha = 1.35$; red solid line). The power-law fitting includes masses up to the peak of the CMF, $\gtrsim 0.6\,M_\odot$. If the next bin is used instead, $\gtrsim 0.9\,M_\odot$, the power-law index is $\alpha = 1.24 \pm 0.12$. For the whole core population, $\alpha = 1.07 \pm 0.09$ ($\gtrsim 0.6\,M_\odot$; black dashed line). The effect of adding the protostellar cores, which are probably warmer than the assumed *Herschel* dust temperature, is to make the power-law index shallower.

In order to reconcile the power-law indexes measured in the high-mass end of the CMF determined in massive clumps, we propose the following scenario. The early fragmentation in 70 μm dark IRDCs results in a power-law index slightly shallower than Salpeter. The most massive cores can accrete material, growing in mass quite quickly according to the recent finding of Contreras et al. (2018). They determine an accretion rate of $2 \times 10^{-3}\,M_\odot\,\mathrm{yr}^{-1}$ in a relatively massive prestellar core. At this accretion rate, in a core free-fall time of 3.3×10^4 yr, the core can accrete ∼4 times its mass (at a constant rate over the whole period). This accretion rate is ∼2 orders of magnitude higher than those found in low-mass cores, which would cause massive cores to accrete more compared to low-mass cores. Thus, the CMF would become shallower at more-evolved stages of cluster formation, as observed in the studies of Liu et al. (2018a) and Motte et al. (2018). Later on, the high accretion rate cannot be maintained due to feedback and the continuum clump fragmentation would catch up. Thus, at later stages of cluster formation, the high-mass end of the CMF would resemble the IMF, as found by Cheng et al. (2018). We, however, acknowledge the difficulty in comparing the results
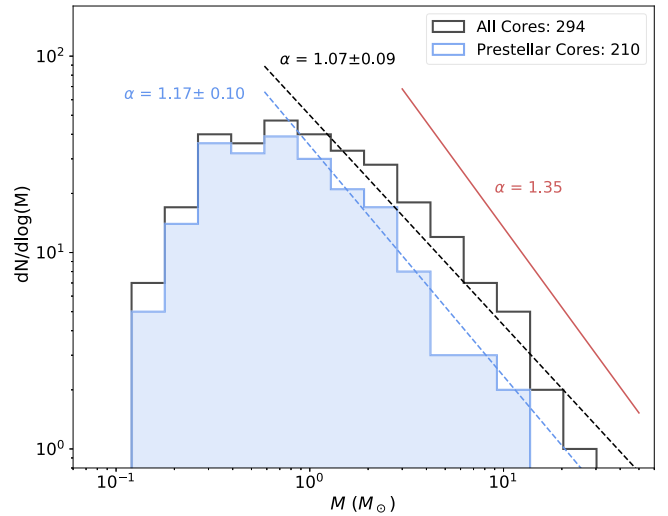

Figure 16. Combined core mass function for the prestellar population, in blue, and for the whole core population, in black. The dashed blue line shows the power-law fitting to the high-mass end for the prestellar population, $\alpha = 1.17 \pm 0.10$, including cores with masses $\gtrsim 0.6\,M_\odot$. The dashed black line shows the power-law fitting to the high-mass end for the complete core population, $\alpha = 1.07 \pm 0.09$, for the same range of core masses. The red solid line shows the Salpeter IMF with $\alpha = 1.35$.

from different works, for example, using different methods for core determination, inclusion/exclusion of the 7 m array, combining prestellar and protostellar cores. A uniform analysis of a large sample can definitively test the proposed scenario, as will be done with ALMA-IMF (ALMA large program; F. Motte et al. 2019, in preparation).

5.7. High-mass Star Formation Picture

We have revealed the early fragmentation and discovered the first members of future stellar clusters that will host high-mass stars. Given the low degree of star formation activity (70 μm dark clumps and only 29% of embedded protostellar cores), protostellar feedback should only play a minor role in these IRDCs. To date, ASHES offers the largest population of prestellar core candidates detected in high-mass clumps. Having characterized a large sample of cores, we are in position to constrain high-mass star formation models.

High-mass prestellar cores, defined here as cores with masses $> 30\,M_\odot$, are the cornerstone of the turbulent core accretion model (McKee & Tan 2003; Tan et al. 2013, 2014). However, they have not been unambiguously found in IRDCs (Zhang et al. 2009, 2015; Wang et al. 2014; Ohashi et al. 2016; Sanhueza et al. 2017; Beuther et al. 2018b; Contreras et al. 2018; Kong et al. 2018b). The case is different in more-evolved high-mass star-forming regions. Whereas some studies find a few rare prestellar high-mass core candidates (Cyganowski et al. 2014; Liu et al. 2017; Nony et al. 2018), other studies find none (e.g., Fontani et al. 2018; Louvet et al. 2019). In ASHES, over 210 prestellar core candidates are detected, with no high-mass prestellar cores detected. The most massive prestellar core has a mass of only $11\,M_\odot$. The fact that the only high-mass prestellar candidates found so far are near other high-mass protostellar objects suggests an environmental dependence, but this raises the question of how the earlier high-mass protostars formed. An alternative view can be that the most massive prestellar cores found at the earliest stages of star formation, such as those IRDC cores in the mass range of 10–20 $M_\odot$ found
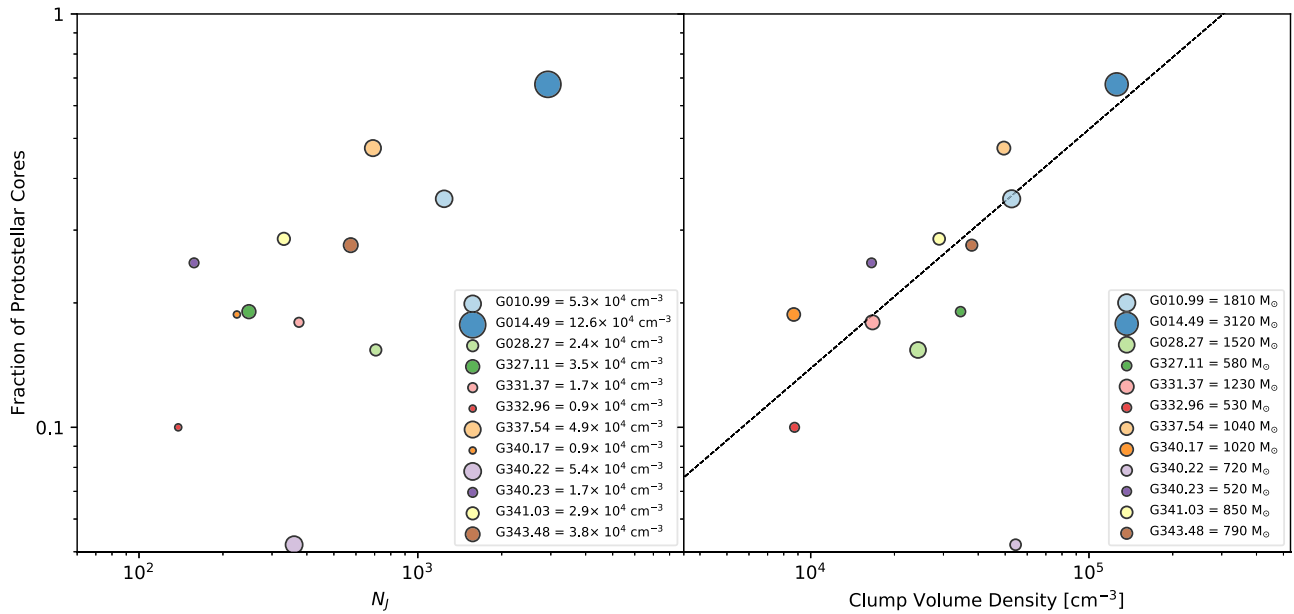
Figure 17. Left: Jeans number, $N_J = M_{cl}/M_J$, vs. the fraction of protostellar cores per clump. A strong correlation with a Spearman correlation coefficient $\rho_s = 0.52$ is measured. After excluding the "outlier" clump with no protostellar cores (G340.222–00.167), the correlation becomes stronger with $\rho_s = 0.6$. Right: clump volume density against the fraction of protostellar cores per clump. The number of protostellar cores scale as $\propto n_{cl}^{\beta}$ with $\beta = 0.57 \pm 0.11$. For display reasons in the log–log plot, we artificially assigned a protostellar fraction of 0.05 to G340.222–00.167.

in the works mentioned above and in ASHES, take time to grow in mass. This is indeed possible in all of the clump-fed scenarios (competitive accretion scenario, Bonnell et al. 2004; Bonnell & Bate 2006; Smith et al. 2009; Wang et al. 2010; global hierarchical collapse, Vázquez-Semadeni et al. 2009, 2017, 2019), considering the accretion rates determined, for now, in a single example (Contreras et al. 2018). With accretion rates of $\sim 10^{-3}\,M_\odot\,\mathrm{yr}^{-1}$, cores can significantly gain mass in a typical clump free-fall time of a few 10^5 yr (Contreras et al. 2016). However, it is unclear if a prestellar core of 10–20 $M_\odot$ can become massive and still remain starless, or if it will first form a low-mass protostar that will then be fed by the growing core. Nevertheless, the absence of high-mass prestellar cores in the early stages of fragmentation of high-mass star-forming regions constrains their formation to only later stages of evolution.

Krumholz & McKee (2008) suggest that to allow the formation of high-mass stars and avoid "excessive" fragmentation, cores should have both surface densities $\Sigma \gtrsim 1\,\mathrm{g\,cm}^{-2}$ and be heated by accreting surrounding protostars in order to increase the Jeans mass. Such heating has not been observed so far (Zhang et al. 2009; Wang et al. 2012; Sanhueza et al. 2017). According to Tan et al. (2013), magnetically mediated high-mass star formation (e.g., Commerçon et al. 2011; Myers et al. 2013) would not require a minimum Σ and lower values, e.g., $\sim 0.5\,\mathrm{g\,cm}^{-2}$, would be sufficient. We find that 89 (30%) cores of all masses have $\Sigma > 0.5\,\mathrm{g\,cm}^{-2}$, including the 16 most massive cores.

We detect for the first time a large population of low-mass cores ($\lesssim 1\,M_\odot$) evolving along with the seeds that will form high-mass stars. Studies of cluster formation made with a single pointing or excluding the 7 m array may well miss a large portion of the low-mass cluster members and, on occasion, even the most massive ones. The whole core population is quite consistent with thermal Jeans fragmentation with masses smaller than or similar to the Jeans mass and separations comparable to or larger (within a factor of 2) than the Jeans length. Turbulent

Jeans fragmentation cannot explain the initial fragmentation observed in these IRDCs. We note that similar results have been also found in more-evolved stages of high-mass star formation (Palau et al. 2015; Beuther et al. 2018a; Svoboda et al. 2019), further confirming the irrelevance of turbulent Jeans fragmentation in the formation of high-mass stars and cluster formation. In general, a low-mass population of prestellar cores in clumps at early stages of evolution is more consistent with competitive accretion and global hierarchical collapse scenarios. Specifically, simulations run by Smith et al. (2009) result in good agreement with our observations. They found in the simulations an average prestellar core mass and radius of 0.7 $M_\odot$ and 2.4×10^3 au at the moment the cores first become bound (total of 306 objects throughout the lifetime of the simulation). The maximum prestellar (bound) core mass reached that is able to form a high-mass star, throughout the whole simulation, is 6.35 $M_\odot$. In our survey, the mean prestellar core mass and radius are 1.2 $M_\odot$ and 2.9×10^3 au, with a maximum prestellar core mass of 11 $M_\odot$. The difference in the radii for the observations and simulations is rather small ($\sim 20\%$), while for the mass, the observed values (mean and maximum mass) are a factor of 1.7 larger. The mean values are measured in the simulations at the moment cores become bound. In the competitive accretion scenario, it is expected that the cores will grow in mass (and likely in size) and may be possible that the masses approach the observed values later on. On the other hand, the smaller mass of the most massive prestellar core in the simulation may reflect the absence of magnetic fields in the simulation. Magnetic fields have been suggested to halt fragmentation, making the mass of the fragments/cores larger (Commerçon et al. 2011).

Vázquez-Semadeni et al. (2019) claim that a natural consequence of the global hierarchical collapse scenario is that the fragmentation level, measured as the total number of cores (protostellar plus prestellar cores), is directly proportional to the Jeans number or the root square of clump density ($N_J = M_{cl}/M_J \propto n_{cl}^{1/2}$). Such a correlation has been observed

in more-evolved intermediate-/high-mass star-forming regions by, for example, Palau et al. (2014, 2015). However, Vázquez-Semadeni et al. (2019) predict that this correlation would be present in an advanced stage after the global collapse has started, once most of the fragmentation epochs have occurred. Therefore, it is expected that the correlation would be weak or absent at the earliest stages of high-mass star formation. We searched for this correlation and found a Spearman's coefficient $\rho_s = 0.33$ for the number of cores versus N_J and $\rho_s = 0.44$ for the number of cores versus $n_{cl}^{1/2}$, indicating a moderate correlation, in agreement with the global hierarchical collapse scenario prediction. Interestingly, we find a strong correlation between the fraction of protostellar cores and N_J. This correlation is shown in Figure 17 and both completely independent quantities correlate with $\rho_s = 0.52$ ($\rho_s = 0.6$, excluding the prestellar clump). This correlation is in better agreement with the findings of Palau et al. (2014, 2015), considering that their cores were mostly protostellar. According to Vázquez-Semadeni et al. (2019), in the global hierarchical collapse scenario, such a correlation is expected. Clumps start gravitational collapse at a given density that defines a Jeans mass, but as time moves forward, the clump density increases, decreasing the corresponding Jeans mass and increasing the number of Jeans masses over time. Therefore, clumps with a larger number of Jeans masses would be more evolved, presenting a larger fraction of protostellar cores that would be inversely proportional to the clump free-fall time. As a result, the fraction of protostellar cores should scale with $\propto n_{cl}^{1/2}$. We indeed find that the fraction of protostellar cores scale as $\propto n_{cl}^{\beta}$ with $\beta = 0.57 \pm 0.11$, consistent with the theoretical prediction, within the uncertainties.

The spatial core distribution, characterized by $\mathcal{Q}$ values from 0.63 to 0.80, is found to be consistent with hierarchical subclustering rather than centrally peaked clustering. Maschberger et al. (2010) analyzed two cluster formation simulations, one of them of a $10^3\,M_\odot$ clump with 1 pc diameter made by Bonnell et al. (2003). Using the MST method in a similar fashion as done here, Maschberger et al. (2010) found that the whole cluster spatial distribution is characterized by a monotonic increase in $\mathcal{Q}$ values, starting at early times with $\sim$0.5 and evolving to >1 at the end of the simulation. The $\mathcal{Q}$ values obtained in the simulation are consistent with our observations. Given that we are tracing only the very early stages of high-mass star formation, the range of observed $\mathcal{Q}$ values is restricted to the values obtained at the beginning of the simulation. However, we do find a weak correlation (that becomes stronger after removing the outlier) of increasing $\mathcal{Q}$ with star formation activity, traced by the fraction of protostellar cores.

Based on the premise that the cores near the center of the gravitational potential accrete more material than cores located at other positions in the cluster, competitive accretion scenarios predict primordial mass segregation (Bonnell & Davies 1998; Bonnell & Bate 2006). Maschberger et al. (2010) also calculated the mass segregation ratio (Λ_{MSR}), finding values of 2–3 over the 10 most massive members by the end of the simulations ($\sim$0.5 Myr). They state that, because the simulation corresponds to a deeply embedded phase of star formation, the mass segregation derived is primordial. They conclude that the most massive sinks are segregated for subcluters with over 30 members. Mass segregation has also been found in simulations that are consistent with the analytical turbulent core accretion model (Myers et al. 2014). At least at the evolutionary phase traced in ASHES, we find no strong indication of primordial mass segregation produced by the

fragmentation itself. However, we cannot rule out the possibility that due to accretion, the members now near the center of the gravitational potential will become the most massive cores in the future because of their privileged location in the forming cluster.

In the context of the turbulent core accretion model, the stellar mass is related by an approximately constant star formation efficiency to the core mass. Consequently, the IMF is predicted to be the result of the prestellar CMF (McKee & Tan 2003; Tan et al. 2014; Cheng et al. 2018), and the efficiency factor is regulated mostly by outflow feedback (Matzner & McKee 2000) and later on by radiative feedback from the high-mass stars (Tanaka et al. 2017). We therefore would expect to find a Salpeter power-law index in the high-mass tail of the prestellar CMF. On the other hand, this mapping of the CMF into the IMF, i.e., a correspondence of core to star, ignores the influence of environmental factors on the core during the accretion process (Smith et al. 2009). Clump-fed scenarios would thus have power-law indexes different from Salpeter in the prestellar CMF that would evolve into Salpeter at the end of cluster formation (e.g., Clark et al. 2007). We find a power-law index of 1.17 ± 0.10 at the high-mass end ($>0.6\,M_\odot$), which is slightly, but significantly, shallower than Salpeter. This may suggest some link between the early CMF and the final IMF. However, current evidence from more-evolved sites of high-mass star formation indicates that the power-law index could evolve. Intermediate-stage high-mass star-forming regions (Liu et al. 2018a; Motte et al. 2018) have power-law indexes of $\sim$0.9, while in more-evolved stages of protocluster formation (Cheng et al. 2018), the CMF appears to be Salpeter. The lack of a constant similarity between the CMF and the IMF over the lifetime of high-mass cluster formation may indicate that in high-mass star-forming regions, the core masses are not the main gas reservoir for forming stars, in opposition to predictions from the turbulent core accretion scenario. Instead, global clump infall would increase core masses and provide most of the material that ultimately makes up stars. The growing evidence of global collapse observed over hundreds of massive clumps supports this hypothesis (He et al. 2015, 2016; Jackson et al. 2019). For now, it is unclear if competitive accretion scenarios can explain the few CMFs measured in high-mass star-forming regions observed so far. Clark et al. (2007) argued that due to different lifetimes for low- and high-mass cores, the CMF would need to be shallower to reproduce the IMF. However, the power-law index would need to be much lower than has been observed (<0.5) and it is unclear which core lifetime would be longer. Maschberger et al. (2010) showed that in the Bonnell et al. (2003) simulation, the IMF for sink particles has a power-law index that smoothly decreases from 1.6 to 0.8 over 3×10^5 yr. This is partially consistent with the scenario proposed here that early on, the CMF at the high-mass end resembles the Salpeter IMF and then becomes shallower due to differential accretion depending on the core mass. However, the simulations do not show if at later times the IMF for sink particles increases to reconcile with the Salpeter IMF. Although the CMF measurements in high-mass star-forming regions are still scarce, this is expected to change with the surveys that are currently being observed with ALMA. A more complete understanding of the link or lack of connection between the CMF and the IMF will also require simulations that can cover evolutionary stages similar to those observed.

Overall, based on the present study, a complete theory of high-mass star formation should reproduce the characteristics of the very early stages of evolution discussed here: (i) absence

of high-mass prestellar cores, (ii) large population of low-mass cores, (iii), hierarchical subclustering, (iv) absence of primordial mass segregation, and (v) slightly shallower CMF than the Salpeter IMF slope in the high-mass tail.

6. Conclusions

We presented the first results of ASHES (the ALMA Survey of 70 μm dark High-mass clumps in Early Stages), a program aimed to characterize the elusive early stages of high-mass star formation to constrain high-mass star formation theories. In the pilot survey, we have mosaicked 12 massive IRDC clumps with ALMA in continuum and line emission, including both 12 and 7 m arrays and total power. In this study, we presented the survey and analyzed the dust continuum emission to draw the following conclusions:

1. We successfully detected cores in all 12 massive IRDC clumps. A total of 294 cores are discovered and classified as protostellar (84; 29%), if they are associated with outflow activity or warm line emission, and as prestellar (210; 71%), if they lack of any star formation signatures. We conclude that eleven of twelve 70 μm dark clumps have nascent, but deeply embedded, star formation activity. However, the revealed star formation activity is from low-mass protostars likely forming along with the seeds that will eventually become high-mass protostars. These seeds could be in the form of prestellar cores or growing low-mass protostars. The number of detected cores is independent of the 3.5σ threshold used to define a core. On average, the most massive clumps tend to form more cores.

2. A large population of low-mass cores ($<1\,M_\odot$) is detected evolving along with the seeds that will form high-mass stars, which is consistent with the competitive accretion and the global hierarchical collapse scenarios. No high-mass prestellar cores ($>30\,M_\odot$) are detected, constraining the formation of high-mass prestellar cores predicted in the turbulent core accretion scenario to only later times in the cluster formation. The most massive prestellar cores have $11\,M_\odot$, which corresponds to five times the Jeans mass. The most massive prestellar cores in each clump are likely to continue accreting material and growing in mass to finally form a high-mass star (e.g., Contreras et al. 2018), as suggested theoretically by the competitive accretion and global hierarchical collapse scenarios, and the growing observational evidence of large numbers of massive clumps under global collapse. Therefore, it is likely that the seeds that will form high-mass stars are formed early on, but the high-mass star itself forms later as the whole clump evolves. However, it is unclear if the cores will reach a "high-mass status" as prestellar or with an embedded low-mass protostar located at their centers. We also find that the most massive cores have surface densities ($>0.5\,\mathrm{g\,cm^{-2}}$) consistent with the predictions of turbulent core accretion.

3. To characterize the core separation, we used the MST technique. The average minimum separation between cores, as defined by the MST, is comparable to or larger (within a factor 2) than the derived Jeans length for each clump. While the observations of these clumps at early evolutionary stages reveal a large range of core masses and core separations, the mean masses and mean separations are consistent with the thermal Jeans fragmentation. Turbulent Jeans lengths are typically larger than the observed core separations, and the turbulent Jeans masses are orders of magnitude higher. Turbulent Jeans fragmentation is therefore ruled out by these observations.

4. Making use of the MST and the $\mathcal{Q}$ parameter, we found that the spatial core distribution follows hierarchical subclustering

rather than centrally peaked clustering. With $\mathcal{Q}$ values ranging from 0.63 to 0.80, we find a weak correlation between the $\mathcal{Q}$ value and star formation activity in the clumps (traced by the fraction of protostellar cores). The range of $\mathcal{Q}$ values and the trend are both consistent with competitive accretion simulations.

5. Using mass segregation ratios (Λ_{MSR} and Γ_{MSR}), we searched for primordial mass segregation. Eight clumps are fully consistent with an equal spatial distribution of low/massive cores ($\Lambda_{\mathrm{MSR}} \approx \Gamma_{\mathrm{MSR}} \approx 1$). The other four clumps have segregation ratios departing from unity, but only with a low number (two or three) of massive members clustered together. The low number of clustered massive cores makes the results strongly sensitive to the temperature assumption used for mass determination. We conclude that there is no solid evidence of primordial mass segregation, in direct contrast to the predictions of competitive accretion theory. However, we cannot rule out that later in the evolution of the clumps, accretion into the cores rather than dynamical effects may produce core mass segregation.

6. We constructed the CMF by combining all prestellar cores detected in each clump. The high-mass end has a power-law index of 1.17 ± 0.10, which is slightly shallower than the Salpeter index for the IMF. Placing in context this work with (scarce) previous works in other more-evolved high-mass star-forming regions, we propose that the CMF at early times is nearly Salpeter (but shallower), then it evolves into a significantly shallower CMF, due to the larger accretion rates of the most massive members, to then become Salpeter again once accretion for the massive members has ceased and due to a continuous clump fragmentation producing new (mostly) low-mass cores. This scenario and the current observational evidence on the variations of the power-law index over the clump evolution suggest a dynamical high-mass star formation picture. The core masses are not the main gas reservoir to form stars, and accretion plays an important role in shaping the final IMF, which is in opposition to the prediction from the turbulent core accretion theory. Competitive accretion and global hierarchical collapse theories predict variations on the power-law index, but it is unclear if they agree with the proposed scenario. Larger samples over different evolutionary stages and more simulations tracing the evolution of the power-law index are necessary to fully understand the origin of the IMF.

In this study, we put firm constraints on the earliest stages of high-mass star formation and we expect to refine them once the whole survey is analyzed. We finally conclude that a complete high-mass star formation theory should reproduce the general features presented in this work, as well as the core dynamics (virial equilibrium, nonthermal component, Mach number, core-to-core velocity dispersion) presented in Y. Contreras et al. (2019, in preparation). We acknowledge that the whole observational picture will not be complete until we constrain the magnetic field at the early stages of high-mass star formation.

Appendix A
Derivation of the Maximum Stellar Mass Using the IMF

Here we refine the derivation presented in Sanhueza et al. (2017). Compared with the previous derivation, we added the lowest mass regime of the IMF from Kroupa (2001) as follows:

$\xi(m) \propto m^{-0.3}$ for $0.01\,M_\odot \leqslant m < 0.08\,M_\odot$, $\xi(m) \propto m^{-1.3}$ for $0.08\,M_\odot \leqslant m < 0.5\,M_\odot$, and $\xi(m) \propto m^{-2.3}$ for $m \geqslant 0.5\,M_\odot$, where m corresponds to the star's mass and $\xi(m)dm$ is the number of stars in the mass interval m to $m + dm$. Therefore Equations (A4) and (A5) from Sanhueza et al. (2017) are updated to:

$$m_{\max} = \left(\frac{0.3}{\epsilon_{\mathrm{sfe}}} \frac{21.0}{(M_{\mathrm{clump}}/M_\odot)} + 1.5 \times 10^{-3} \right)^{-0.77} M_\odot, \quad (12)$$

and

$$M_{\mathrm{clump}} = \frac{0.3}{\epsilon_{\mathrm{sfe}}} \frac{21.0}{((m_{\max}/M_\odot)^{-1.3} - 1.5 \times 10^{-3})} M_\odot \quad (13)$$

where $m_{\max}$ is the maximum stellar mass (assuming $m_{\max} \geqslant 0.5\,M_\odot$), ϵ_{sfe} is the star formation efficiency with a fiducial value of 30%, and M_{clump} is the clump mass. For $m_{\max} = 8\,M_\odot$, the necessary clump mass to form a high-mass star is $320\,M_\odot$.

Appendix B
Additional Figures

Figure 18 gives more details on Figure 13. In Figure 18, the data are color-coded by clump to show that the correlation is found per individual clump.

In this work, core temperatures were assumed to be the same as their host clump. Figure 13 shows the distribution of core properties, and differences can be seen among the evolutionary
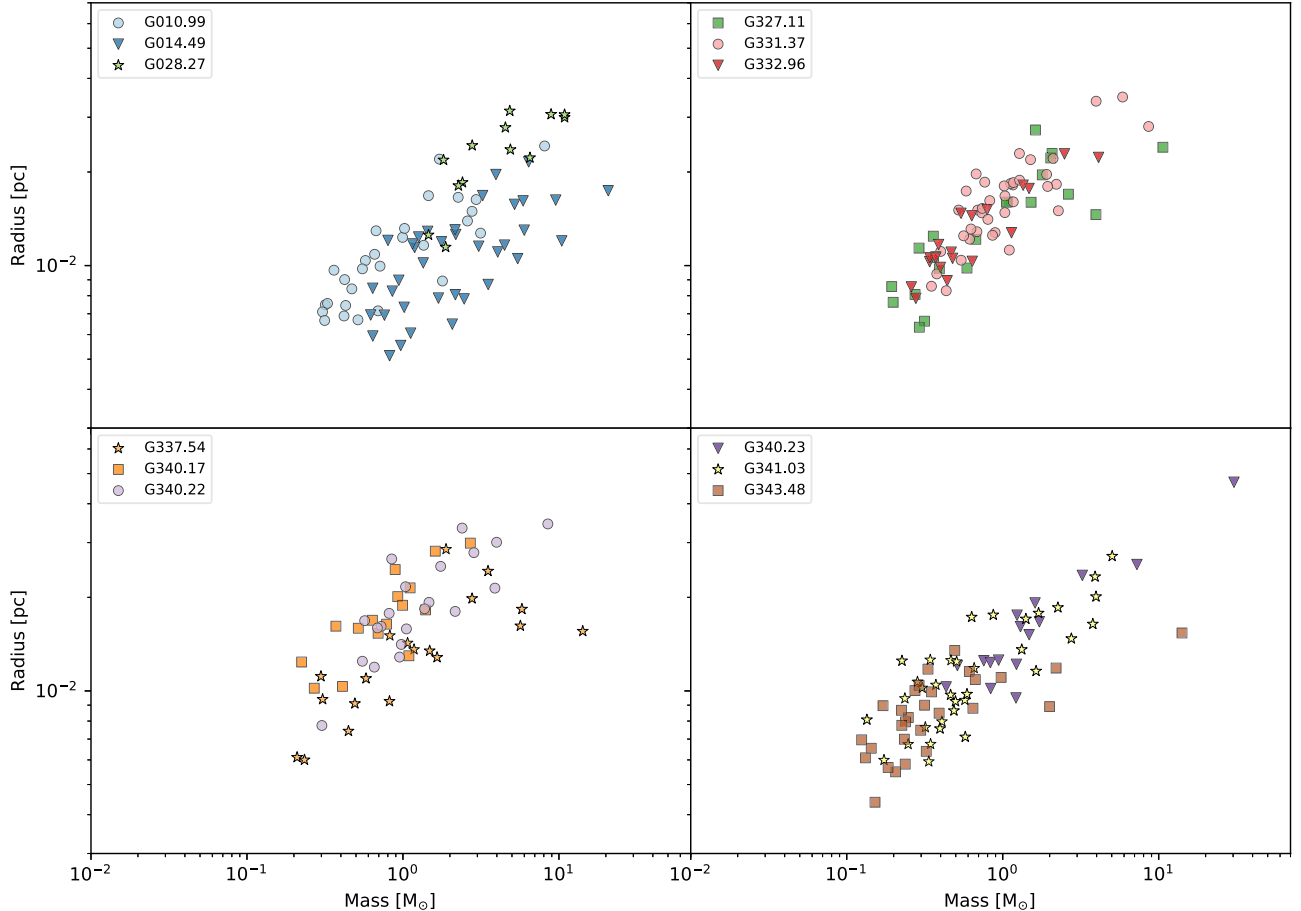

Figure 18. Core radius against the core mass color-coded by clump. The purpose of these scatter plots is to show that for all cores embedded in a clump, i.e., at the same distance, the core radius correlates with the core mass.
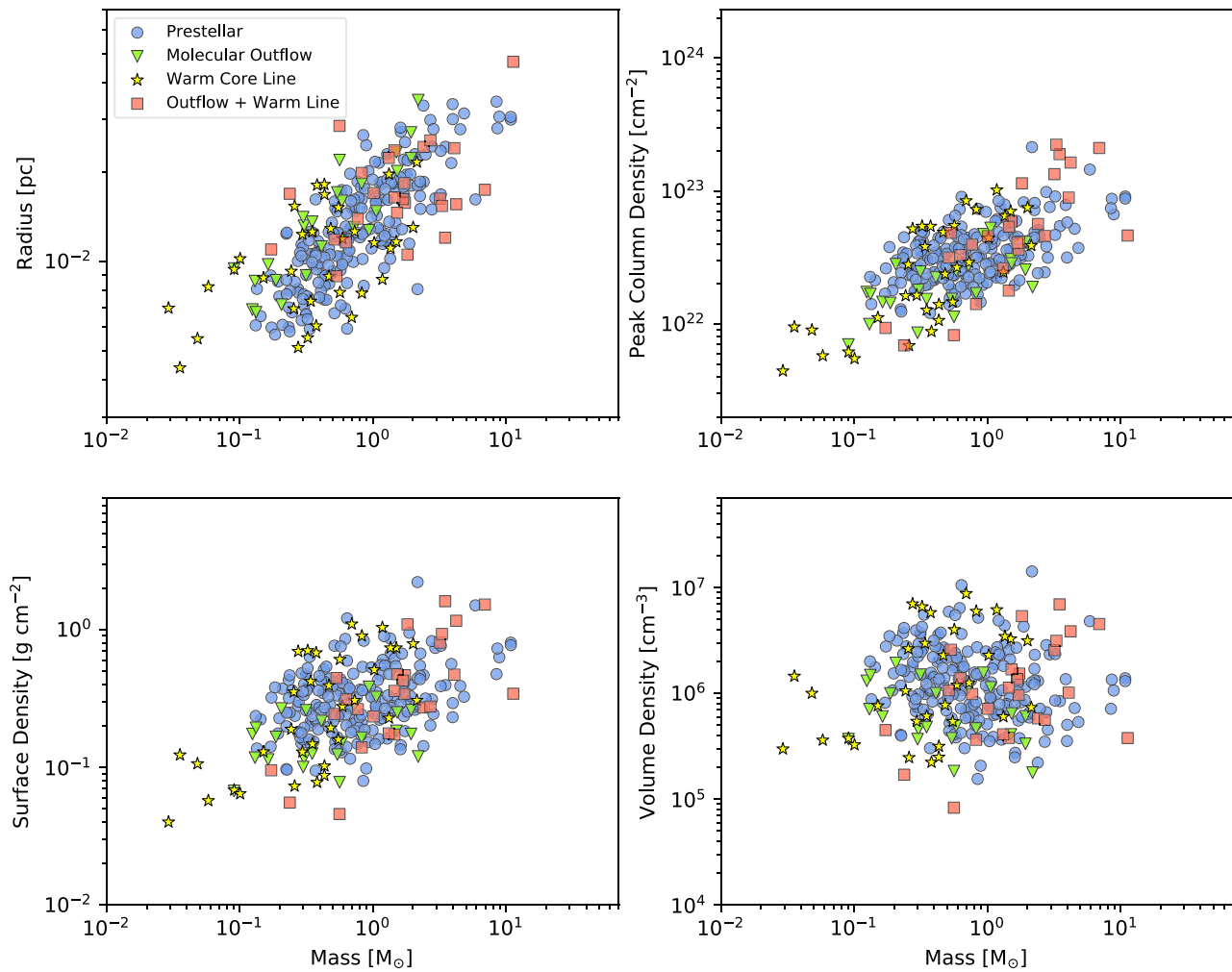
Figure 19. Radius, peak column, surface density, and volume density of cores against the core mass color-coded by protostellar activity (prestellar, molecular outflow only, warm core line only, and both protostellar indicators; see Section 4.3). The purpose of these scatter plots is to show the distribution of core properties by increasing the protostellar core temperatures to 30 K, which is about a factor of 2 larger than the originally assumed clump temperature.

stages. However, protostellar cores are likely warmer and differences in Figure 13 could be produced by the assumed temperature. In Figure 19, we test the effect of temperature by assuming 30 K for protostellar cores. Differences in cores at different evolutionary stages almost disappear.

ORCID iDs

Patricio Sanhueza https://orcid.org/0000-0002-7125-7685
Yanett Contreras https://orcid.org/0000-0002-6388-3635
Benjamin Wu https://orcid.org/0000-0003-3874-7030
James M. Jackson https://orcid.org/0000-0002-3466-6164
Andrés E. Guzmán https://orcid.org/0000-0003-0990-8990
Qizhou Zhang https://orcid.org/0000-0003-2384-6589
Xing Lu https://orcid.org/0000-0003-2619-9305
Andrea Silva https://orcid.org/0000-0001-9500-604X
Natsuko Izumi https://orcid.org/0000-0003-1604-9127
Tie Liu https://orcid.org/0000-0002-5286-2564
Rie E. Miura https://orcid.org/0000-0001-8187-7856
Ken'ichi Tatematsu https://orcid.org/0000-0002-8149-8546
Takeshi Sakai https://orcid.org/0000-0003-4521-7492
Henrik Beuther https://orcid.org/0000-0002-1700-090X
Masao Saito https://orcid.org/0000-0003-0769-8627
Fumitaka Nakamura https://orcid.org/0000-0001-5431-2294

References

Allison, R. J., Goodwin, S. P., Parker, R. J., et al. 2009, MNRAS, 395, 1449
Alves, J., Lombardi, M., & Lada, C. J. 2007, A&A, 462, L17
André, P., Men'shchikov, A., Bontemps, S., et al. 2010, A&A, 518, L102
Avison, A., Peretto, N., Fuller, G. A., et al. 2015, A&A, 577, A30
Ballesteros-Paredes, J., Hartmann, L. W., Vázquez-Semadeni, E., et al. 2011a, MNRAS, 411, 65
Ballesteros-Paredes, J., Vázquez-Semadeni, E., Gazol, A., et al. 2011b, MNRAS, 416, 1436
Ballesteros-Paredes, J., Vázquez-Semadeni, E., Palau, A., et al. 2018, MNRAS, 479, 2112
Barrow, J. D., Bhavsar, S. P., & Sonoda, D. H. 1985, MNRAS, 216, 17
Bastian, N., Covey, K. R., & Meyer, M. R. 2010, ARA&A, 48, 339
Battersby, C., Bally, J., Jackson, J. M., et al. 2010, ApJ, 721, 222
Benjamin, R. A., Churchwell, E., Babler, B. L., et al. 2003, PASP, 115, 953
Beuther, H., Henning, T., Linz, H., et al. 2015, A&A, 581, A119
Beuther, H., Mottram, J. C., Ahmadi, A., et al. 2018a, A&A, 617, A100
Beuther, H., Soler, J. D., Vlemmings, W., et al. 2018b, A&A, 614, A64
Bonnell, I. A., & Bate, M. R. 2006, MNRAS, 370, 488
Bonnell, I. A., Bate, M. R., & Vine, S. G. 2003, MNRAS, 343, 413
Bonnell, I. A., Clark, P., & Bate, M. R. 2008, MNRAS, 389, 1556
Bonnell, I. A., & Davies, M. B. 1998, MNRAS, 295, 691
Bonnell, I. A., Vine, S. G., & Bate, M. R. 2004, MNRAS, 349, 735
Bontemps, S., Motte, F., Csengeri, T., & Schneider, N. 2010, A&A, 524, A18
Busquet, G., Zhang, Q., Palau, A., et al. 2013, ApJL, 764, L26
Butler, M. J., & Tan, J. C. 2009, ApJ, 696, 484
Carey, S. J., Noriega-Crespo, A., Mizuno, D. R., et al. 2009, PASP, 121, 76
Cartwright, A., & Whitworth, A. P. 2004, MNRAS, 348, 589

Caselli, P., Pineda, J. E., Zhao, B., et al. 2019, ApJ, 874, 89
Chambers, E. T., Jackson, J. M., Rathborne, J. M., & Simon, R. 2009, ApJS, 181, 360
Chen, H.-R. V., Zhang, Q., Wright, M. C. H., et al. 2019, ApJ, 875, 24
Cheng, Y., Tan, J. C., Liu, M., et al. 2018, ApJ, 853, 160
Chini, R., Hoffmeister, V. H., Nasseri, A., Stahl, O., & Zinnecker, H. 2012, MNRAS, 424, 1925
Clark, P. C., Klessen, R. S., & Bonnell, I. A. 2007, MNRAS, 379, 57
Cohen, J. 1988, Statistical Power Analysis for the Behavioral Sciences (Hillsdale, NJ: L. Erlbaum Associates)
Commerçon, B., Hennebelle, P., & Henning, T. 2011, ApJL, 742, L9
Contreras, Y., Garay, G., Rathborne, J. M., et al. 2016, MNRAS, 456, 2041
Contreras, Y., Rathborne, J. M., Guzman, A., et al. 2017, MNRAS, 466, 340
Contreras, Y., Sanhueza, P., Jackson, J. M., et al. 2018, ApJ, 861, 14
Contreras, Y., Schuller, F., Urquhart, J. S., et al. 2013, A&A, 549, A45
Csengeri, T., Bontemps, S., Wyrowski, F., et al. 2017, A&A, 600, L10
Csengeri, T., Bontemps, S., Wyrowski, F., et al. 2018, A&A, 617, A89
Cyganowski, C. J., Brogan, C. L., Hunter, T. R., et al. 2014, ApJL, 796, L2
Cyganowski, C. J., Brogan, C. L., Hunter, T. R., et al. 2017, MNRAS, 468, 3694
Dib, S., & Henning, T. 2019, A&A, 629, 135
Feng, S., Beuther, H., Zhang, Q., et al. 2016a, A&A, 592, A21
Feng, S., Beuther, H., Zhang, Q., et al. 2016b, ApJ, 828, 100
Fontani, F., Commerçon, B., Giannetti, A., et al. 2018, A&A, 615, A94
Foster, J. B., Arce, H. G., Kassis, M., et al. 2014, ApJ, 791, 108
Foster, J. B., Jackson, J. M., Barnes, P. J., et al. 2011, ApJS, 197, 25
Foster, J. B., Rathborne, J. M., Sanhueza, P., et al. 2013, PASA, 30, e038
Guzmán, A. E., Sanhueza, P., Contreras, Y., et al. 2015, ApJ, 815, 130
He, Y.-X., Zhou, J.-J., Esimbek, J., et al. 2015, MNRAS, 450, 1926
He, Y.-X., Zhou, J.-J., Esimbek, J., et al. 2016, MNRAS, 461, 2288
Heitsch, F., Hartmann, L. W., Slyz, A. D., et al. 2008, ApJ, 674, 316
Henshaw, J. D., Caselli, P., Fontani, F., et al. 2016, MNRAS, 463, 146
Henshaw, J. D., Caselli, P., Fontani, F., Jiménez-Serra, I., & Tan, J. C. 2014, MNRAS, 440, 2860
Hogge, T., Jackson, J., Stephens, I., et al. 2018, ApJS, 237, 27
Hoq, S., Jackson, J. M., Foster, J., et al. 2013, ApJ, 777, 157
Jackson, J. M., Contreras, Y., Rathborne, J. M., et al. 2018, ApJ, 869, 102
Jackson, J. M., Rathborne, J. M., Foster, J. B., et al. 2013, PASA, 30, e057
Jackson, J. M., Whitaker, J. S., Rathborne, J. M., et al. 2019, ApJ, 870, 5
Juvela, M., Guillet, V., Liu, T., et al. 2018, A&A, 620, A26
Kauffmann, J., & Pillai, T. 2010, ApJL, 723, L7
Kong, S., Arce, H. G., José Maureira, M., et al. 2019, ApJ, 874, 104
Kong, S., Tan, J. C., Arce, H. G., et al. 2018a, ApJL, 855, L25
Kong, S., Tan, J. C., Caselli, P., et al. 2016, ApJ, 821, 94
Kong, S., Tan, J. C., Caselli, P., et al. 2017, ApJ, 834, 193
Kong, S., Tan, J. C., Caselli, P., et al. 2018b, ApJ, 867, 94
Könyves, V., André, P., Men'shchikov, A., et al. 2015, A&A, 584, A91
Kouwenhoven, M. B. N., Brown, A. G. A., Zinnecker, H., Kaper, L., & Portegies Zwart, S. F. 2005, A&A, 430, 137
Kroupa, P. 2001, MNRAS, 322, 231
Kroupa, P., Weidner, C., Pflamm-Altenburg, J., et al. 2013, in Planets, Stars and Stellar Systems, ed. T. D. Oswalt & G. Gilmore (Dordrecht: Springer), 115
Krumholz, M. R., & Bonnell, I. A. 2009, in Structure Formation in Astrophysics, ed. G. Chabrier (Cambridge: Cambridge Univ. Press), 288
Krumholz, M. R., Klein, R. I., & McKee, C. F. 2007, ApJ, 656, 959
Krumholz, M. R., Klein, R. I., & McKee, C. F. 2012, ApJ, 754, 71
Krumholz, M. R., & McKee, C. F. 2008, Natur, 451, 1082
Lada, C. J., & Lada, E. A. 2003, ARA&A, 41, 57
Larson, R. B. 2003, in ASP Conf. Ser. 287, Galactic Star Formation Across the Stellar Mass Spectrum, ed. J. M. De Buizer & N. S. van der Bliek (San Francisco, CA: ASP), 65
Li, S., Wang, J., Fang, M., et al. 2019b, ApJ, 878, 29
Li, S., Zhang, Q., Pillai, T., et al. 2019a, arXiv:1909.08916
Li, M., Zhou, J., Esimbek, J., et al. 2019c, ApJS, 243, 13
Li, Q., Zhou, J., Esimbek, J., et al. 2019d, MNRAS, 488, 4638
Liu, M., Tan, J. C., Cheng, Y., & Kong, S. 2018a, ApJ, 862, 105
Liu, T., Kim, K.-T., Juvela, M., et al. 2018b, ApJS, 234, 28
Liu, T., Lacy, J., Li, P. S., et al. 2017, ApJ, 849, 25
Liu, T., Li, P. S., Juvela, M., et al. 2018c, ApJ, 859, 151
Liu, X.-L., Wang, J.-J., & Xu, J.-L. 2014, MNRAS, 443, 2264
Longmore, S. N., Pillai, T., Keto, E., Zhang, Q., & Qiu, K. 2011, ApJ, 726, 97
Louvet, F., Neupane, S., Garay, G., et al. 2019, A&A, 622, A99
Lu, X., Zhang, Q., Liu, H. B., et al. 2018, ApJ, 855, 9
Lu, X., Zhang, Q., Wang, K., & Gu, Q. 2015, ApJ, 805, 171

Maschberger, T., Clarke, C. J., Bonnell, I. A., & Kroupa, P. 2010, MNRAS, 404, 1061
Matzner, C. D., & McKee, C. F. 2000, ApJ, 545, 364
McKee, C. F., & Tan, J. C. 2003, ApJ, 585, 850
McMullin, J. P., Waters, B., Schiebel, D., et al. 2007, adass XVI, 127
Miettinen, O. 2014, A&A, 562, A3
Molinari, S., Swinyard, B., Bally, J., et al. 2010, A&A, 518, L100
Motte, F., Nony, T., Louvet, F., et al. 2018, NatAs, 2, 478
Myers, A. T., Klein, R. I., Krumholz, M. R., & McKee, C. F. 2014, MNRAS, 439, 3420
Myers, A. T., McKee, C. F., Cunningham, A. J., Klein, R. I., & Krumholz, M. R. 2013, ApJ, 766, 97
Nony, T., Louvet, F., Motte, F., et al. 2018, A&A, 618, L5
Ohashi, S., Sanhueza, P., Chen, H.-R. V., et al. 2016, ApJ, 833, 209
Ohashi, S., Sanhueza, P., Sakai, N., et al. 2018, ApJ, 856, 147
Olczak, C., Spurzem, R., & Henning, T. 2011, A&A, 532, A119
Ossenkopf, V., & Henning, T. 1994, A&A, 291, 943
Palau, A., Ballesteros-Paredes, J., Vázquez-Semadeni, E., et al. 2015, MNRAS, 453, 3785
Palau, A., Estalella, R., Girart, J. M., et al. 2014, ApJ, 785, 42
Parker, R. J., & Goodwin, S. P. 2015, MNRAS, 449, 3381
Peretto, N., & Fuller, G. A. 2009, A&A, 505, 405
Pillai, T., Kauffmann, J., Tan, J. C., et al. 2015, ApJ, 799, 74
Pillai, T., Kauffmann, J., Wyrowski, F., et al. 2011, A&A, 530, A118
Pillai, T., Kauffmann, J., Zhang, Q., et al. 2019, A&A, 622, A54
Pillai, T., Wyrowski, F., Menten, K. M., & Krügel, E. 2006, A&A, 447, 929
Ragan, S. E., Henning, T., Beuther, H., Linz, H., & Zahorecz, S. 2015, A&A, 573, A119
Rathborne, J. M., Jackson, J. M., & Simon, R. 2006, ApJ, 641, 389
Rathborne, J. M., Jackson, J. M., Zhang, Q., & Simon, R. 2008, ApJ, 689, 1141
Rathborne, J. M., Whitaker, J. S., Jackson, J. M., et al. 2016, PASA, 33, e030
Rosero, V., Hofner, P., Claussen, M., et al. 2016, ApJS, 227, 25
Rosero, V., Hofner, P., Kurtz, S., et al. 2019, ApJ, 880, 99
Rosero, V., Hofner, P., McCoy, M., et al. 2014, ApJ, 796, 130
Rosolowsky, E. W., Pineda, J. E., Kauffmann, J., & Goodman, A. A. 2008, ApJ, 679, 1338
Sakai, T., Sakai, N., Foster, J. B., et al. 2013, ApJL, 775, L31
Sakai, T., Sakai, N., Furuya, K., et al. 2012, ApJ, 747, 140
Sakai, T., Sakai, N., Furuya, K., et al. 2015, ApJ, 803, 70
Sakai, T., Sakai, N., Kamegai, K., et al. 2008, ApJ, 678, 1049
Sakai, T., Yanagida, T., Furuya, K., et al. 2018, ApJ, 857, 35
Salpeter, E. E. 1955, ApJ, 121, 161
Sanhueza, P., Garay, G., Bronfman, L., et al. 2010, ApJ, 715, 18
Sanhueza, P., Jackson, J. M., Foster, J. B., et al. 2012, ApJ, 756, 60
Sanhueza, P., Jackson, J. M., Foster, J. B., et al. 2013, ApJ, 773, 123
Sanhueza, P., Jackson, J. M., Zhang, Q., et al. 2017, ApJ, 841, 97
Schuller, F., Menten, K. M., Contreras, Y., et al. 2009, A&A, 504, 415
Shirley, Y. L., Ellsworth-Bowers, T. P., Svoboda, B., et al. 2013, ApJS, 209, 2
Simon, R., Jackson, J. M., Rathborne, J. M., & Chambers, E. T. 2006, ApJ, 639, 227
Smith, R. J., Longmore, S., & Bonnell, I. 2009, MNRAS, 400, 1775
Stephens, I. W., Jackson, J. M., Sanhueza, P., et al. 2015, ApJ, 802, 6
Stephens, I. W., Jackson, J. M., Whitaker, J. S., et al. 2016, ApJ, 824, 29
Svoboda, B. E., Shirley, Y. L., Traficante, A., et al. 2019, arXiv:1908.10374
Tan, J. C. 2018, in IAU Symp. 332, Astrochemistry VII: Through the Cosmos from Galaxies to Planets, ed. M. Cunningham, T. Millar, & Y. Aikawa (Cambridge: Cambridge Univ. press), 139
Tan, J. C., Beltrán, M. T., Caselli, P., et al. 2014, in Protostars and Planets VI, ed. H. Beuther et al. (Tucson, AZ: Univ. Arizona Press), 149
Tan, J. C., Kong, S., Butler, M. J., Caselli, P., & Fontani, F. 2013, ApJ, 779, 96
Tan, J. C., Kong, S., Zhang, Y., et al. 2016, ApJ, 821, L3
Tan, J. C., Krumholz, M. R., & McKee, C. F. 2006, ApJ, 641, L121
Tanaka, K. E. I., Tan, J. C., & Zhang, Y. 2017, ApJ, 835, 32
Tang, Y.-W., Koch, P. M., Peretto, N., et al. 2019, ApJ, 878, 10
Tatematsu, K., Liu, T., Ohashi, S., et al. 2017, ApJS, 228, 12
Traficante, A., Fuller, G. A., Peretto, N., Pineda, J. E., & Molinari, S. 2015, MNRAS, 451, 3089
Urquhart, J. S., Moore, T. J. T., Csengeri, T., et al. 2014, MNRAS, 443, 1555
Vasyunina, T., Vasyunin, A. I., Herbst, E., et al. 2014, ApJ, 780, 85
Vázquez-Semadeni, E., Gómez, G. C., Jappsen, A.-K., Ballesteros-Paredes, J., & Klessen, R. S. 2009, ApJ, 707, 1023
Vázquez-Semadeni, E., González-Samaniego, A., & Colín, P. 2017, MNRAS, 467, 1313
Vázquez-Semadeni, E., Palau, A., Ballesteros-Paredes, J., Gómez, G. C., & Zamora-Avilés, M. 2019, arXiv:1903.1124
Wang, K., Zhang, Q., Testi, L., et al. 2014, MNRAS, 439, 3275

Wang, K., Zhang, Q., Wu, Y., Li, H.-b., & Zhang, H. 2012, ApJL, 745, L30
Wang, K., Zhang, Q., Wu, Y., & Zhang, H. 2011, ApJ, 735, 64
Wang, P., Li, Z.-Y., Abel, T., & Nakamura, F. 2010, ApJ, 709, 27
Wang, Y., Zhang, Q., Rathborne, J. M., Jackson, J., & Wu, Y. 2006, ApJL, 651, L125
Whitaker, J. S., Jackson, J. M., Rathborne, J. M., et al. 2017, AJ, 154, 140
Wienen, M., Wyrowski, F., Menten, K. M., et al. 2015, A&A, 579, A91
Wu, B., Tan, J. C., Christie, D., et al. 2017, ApJ, 841, 88
Yanagida, T., Sakai, T., Hirota, T., et al. 2014, ApJL, 794, L10
Yu, N., & Wang, J.-J. 2015, MNRAS, 451, 2507
Zhang, Q., Wang, K., Lu, X., & Jiménez-Serra, I. 2015, ApJ, 804, 141
Zhang, Q., Wang, Y., Pillai, T., & Rathborne, J. 2009, ApJ, 696, 268